Stratigraphic evidence of relative sea level changes produced by megathrust earthquakes in the Jalisco subduction zone, Mexico. The signature of the 1995 Colima-Jalisco earthquake (M_w 8) as a modern analogue.

Emmanuel Bustamante Fernandez [a b *], Sarah Woodroffe [a], Jeremy M. Lloyd [a], Ian Shennan [a]

[a] Department of Geography, Durham University, Lower Mountjoy, South Road, Durham, DH1 3LE, UK

[b] Department of Earth and Climate Sciences, Tufts University, Medford, MA 02155, USA

* Corresponding author: emmanuel.bustamante@tufts.edu

Abstract

Geological evidence of megathrust earthquakes along the Mexican Pacific coast relies predominantly on tsunami deposits. Records of coseismic relative sea-level changes are scarce even though such evidence can complement and constrain tsunami records, providing information to reconstruct past earthquake rupture dimensions to improve the earthquake hazard assessment of the region. This paper provides the first diatom-based quantitative reconstruction of coastal subsidence along the Mexican subduction zone through the analysis of coastal wetland sediments. We use the stratigraphic signature of the 1995 Colima-Jalisco earthquake (M_w 8.0) as this earthquake is instrumentally well-constrained, allowing us to evaluate our findings and establish approaches to investigate earlier earthquakes. Deposits beneath the wetland Estero Potrero Grande reveal a stratigraphic sequence, < 28 cm beneath the wetland surface, that resembles a signature of rapid submergence. This sequence consists of a horizontal bed of silt with highly humified organic matter abruptly overlain by a horizontal bed of grey silt. The abrupt stratigraphic contact between the two units extends across > 1 km of the wetland. Using ^{14}C ages and ^{137}Cs chronohorizons to build an age-depth model, we estimate the age range (1985 – 2003 CE) and mean age (1995 CE) of this abrupt stratigraphic contact, coincident with the year of the earthquake. Three elemental log-ratios (S/Zn, Br/Zn and Ca/Zn) indicate an abrupt increase of salinity across the stratigraphic contact, which we interpret as marsh submergence recording coseismic coastal subsidence, reflected as relative sea-level rise. Fossil diatom assemblages confirm this trend, and through quantitative approaches we estimate its magnitude (-0.06 ± 0.08 m and -0.11 ± 0.23 m), which is comparable with coastal subsidence measured by geodetic instruments. Our records reveal a millimetric spike of sand, which we interpret as a signature of the tsunami that accompanied this great earthquake. These findings demonstrate that coastal wetland sediments from the Mexican Pacific coast can record tectonic induced relative sea-level changes. This approach can allow us to better understand the long-term spatial and temporal behavior of this subduction zone.

Keywords: Mexican subduction zone, 1995 Colima-Jalisco earthquake, coastal paleoseismology, relative sea-level changes, tsunami, diatoms.

1. Introduction

Active subduction zones have the potential to produce the largest and most destructive earthquakes on Earth. Exceptionally large areas of slip, which cause high moment magnitudes (M_w), can produce catastrophic consequences in coastal areas adjacent to these earthquake ruptures. These impacts result not only from the strong ground shaking, but also from the substantial and long-lasting modifications produced by rapid land-level changes, as reflected by relative sea-level changes (Hamilton & Shennan, 2005), and erosional and depositional processes caused by tsunamis (e.g. Plafker, 1969; Plafker & Savage, 1970). As these coastal modifications are imprinted in the stratigraphy and geomorphology (e.g Plafker, 1969; Plafker & Savage, 1970; Shennan et al., 1999; Zong et al., 2003; Garrett et al., 2013; Monecke et al., 2015), from these records it has been possible to reconstruct long-term sequences of pre-instrumental earthquakes along the tectonically active coast of Japan (Nanayama et al., 2003; Garrett et al., 2016; Fujiwara et al., 2020; Sawai, 2020); Chile (Cisternas et al., 2005; Dura et al., 2017; Garrett et al., 2015; Kempf et al., 2020; León et al., 2023); Thailand (Jankaew et al., 2008; Gouramanis et al., 2017); Indonesia (Monecke et al., 2008; Dura et al., 2011; Rubin et al., 2017); Alaska (Hamilton et al., 2005; Hamilton & Shennan, 2005; Shennan et al., 2013; Briggs et al., 2014; Kelsey et al., 2015; Nelson et al., 2015); and USA (Atwater et al., 1995; Hemphill-Haley, 1996; Kelsey et al., 2005).

The Mexican Pacific coast, from southern Nayarit to Chiapas, is a tectonically active margin where the Rivera and Cocos plates subduct beneath the North American plate (**Figure 1**). Plate convergence induces the high rate of seismicity and crustal deformation, making this region highly susceptible to earthquake and tsunami hazards (Bandy et al., 1999; Ramirez-Herrera & Urrutia-Fucugauchi, 1999; Manea et al., 2013; Dañobeitia et al., 2016). Geological investigations along the Mexican Pacific (**Figure 1**) concentrate on investigating the sedimentary signature of tsunami deposits (e.g. Ramírez-Herrera et al., 2012, 2016; Černý et al., 2015). However, along this margin the presence of anomalous deposits of marine origin onshore is also attributed to tsunamis induced by submarine landslides (e.g. Ramírez-Herrera et al., 2014; Corona & Ramírez-Herrera, 2015; Bógalo et al., 2017) and hurricanes (e.g. Bianchette et al., 2016, 2022). Consequently, if the origin and source of these deposits cannot be discriminated, their use in paleoseismic studies may overestimate the number of seismic events occurred in this subduction zone. Hence, tsunami evidence requires complementary data on abrupt land-level changes to produce reliable evidence of past earthquakes.

Geological records of coseismic land-level changes along the Mexican Pacific coast are spatially and temporally scarce (**Figure 1**). In the domain of the Cocos plate, the vertical distribution of dead intertidal organisms has been used to assess along-strike variations of coseismic uplift caused by the 1985 M_w 8 Michoacan earthquake (Bodin & Klinger, 1986); the 1998 M_w 6.3 Puerto Angel earthquake (Ramírez-Herrera & Orozco, 2002); and the 2020 M_w 7.4 La Crucecita earthquake (Ramírez-Herrera et al., 2021). Although, geomorphological evidence of abrupt coastal uplift exists along the Mexican Pacific coast (Ramirez-Herrera & Urrutia-Fucugauchi, 1999), this type of evidence is spatially fragmented and commonly lack datable material, limiting their ability to identify episodes of regional uplift, produced coseismically, and reconstruct past earthquakes (e.g. Ramírez-Herrera et al., 2004). In this sense, more recent investigations have demonstrated the potential of stratigraphic sequences in coastal wetlands to record uplift and subsidence produced by (pre-) instrumental earthquakes (Ramírez-Herrera et al., 2007, 2009; Castillo-Aja et al., 2019). However, these coastal settings are still understudied and poorly understood in a paleoseismological context.

Here we investigate the deposits of the coastal wetland Estero Potrero Grande, which lies adjacent to the Marabasco river, on the border of the States of Jalisco and Colima. We use a range of sedimentological, geochemical and microfossil techniques to establish the sedimentary features produced by the 1995 Colima-Jalisco earthquake (M_w 8). With good preservation of fossil diatoms, we develop a quantitative diatom-based approach to estimate the magnitude of relative sea level (RSL) rise, induced by coseismic subsidence. These findings permit us to understand the sensitivity of Estero Potrero Grande to record the stratigraphic signature of abrupt coastal subsidence and establish it as a modern analogue to investigate pre-instrumental megathrust earthquakes.

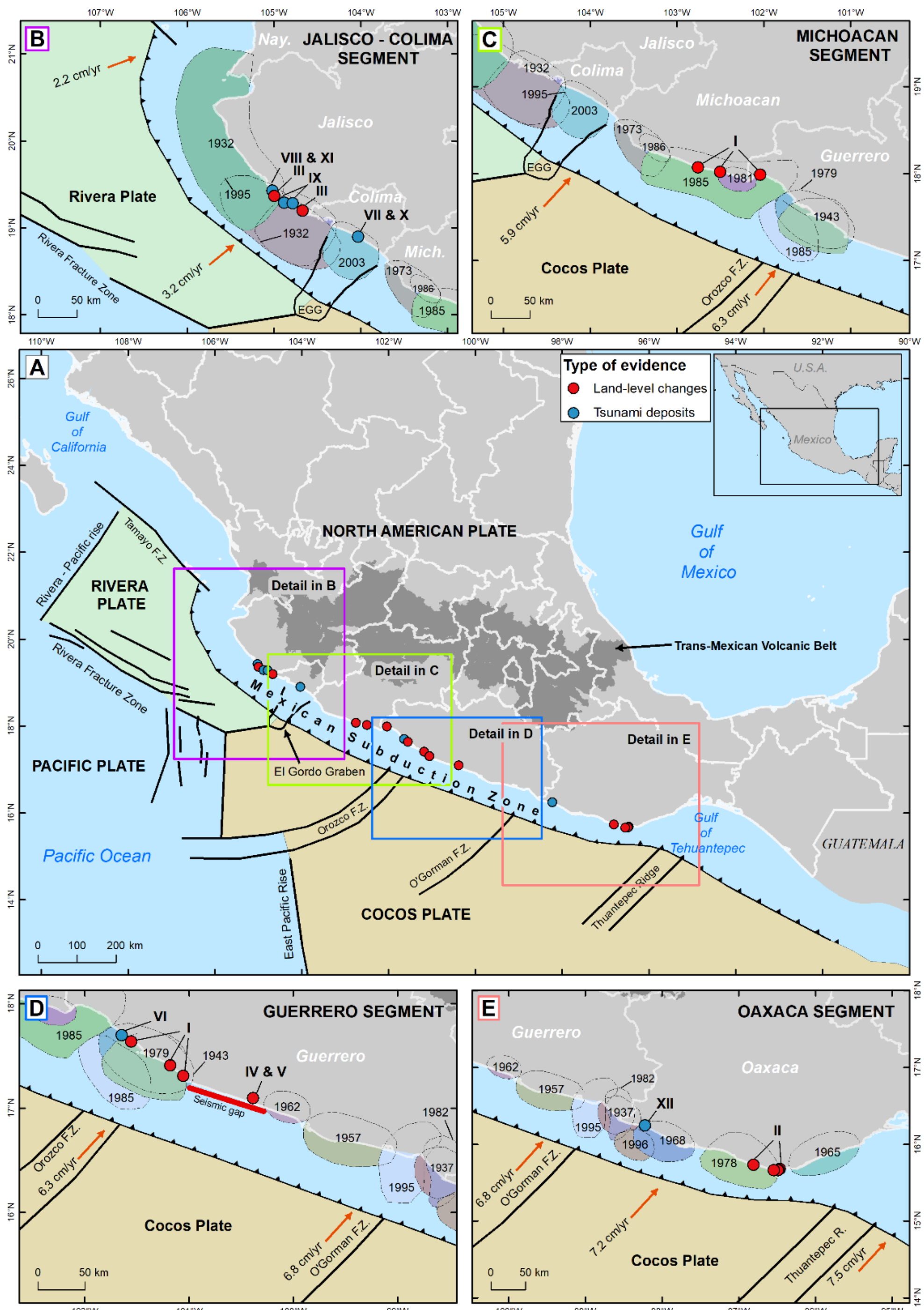

Figure 1. Geological records of past earthquakes along the Mexican Pacific coast. Insets B to E show locations of investigations within along-strike segments proposed by Ramirez-Herrera & Urrutia-Fucugauchi (1999). Ellipses show the rupture areas of those earthquakes recorded instrumentally since the beginning of 1900 (Kostoglodov & Pacheco, 1999). Past studies in chronological order correspond to: I) Bodin & Klinger (1986), II) Ramírez-Herrera & Orozco (2002), III) Ramírez-Herrera et al. (2004), IV) Ramírez-Herrera et al. (2007), V) Ramírez-Herrera et al.

(2009), V) Ramírez-Herrera et al. (2012), VII) Ramírez-Herrera et al. (2014), VIII) Černý et al. (2015), IX) (M. T. Ramírez-Herrera et al., 2016), X) (Bógalo et al., 2017), XI) Castillo-Aja et al. (2019), XII) Ramírez-Herrera et al. (2020).

1.1. The 1995 Colima-Jalisco M_w 8.0 earthquake.

The 9 October 1995 M_w 8 earthquake is the second largest instrumentally recorded megathrust earthquake along the subduction zone of the Rivera and North America plates (**Figures 1 and 2**). It struck 63 years after the sequence of catastrophic earthquakes occurred on 3 June 1932 (M_w 8.2, event 1932-I) and 18 June 1932 (M_w 7.8, event 1932-II). The 1995 earthquake has the peculiarity of being the first megathrust earthquake in the region with coseismic deformation measured using the local network of Global Positioning System (GPS) receivers (Melbourne et al., 1997; Hutton et al., 2001; Hjörleifsdóttir et al., 2018; Cosenza-Muralles et al., 2021a), which began operating just months earlier (DeMets et al., 1995). Geodetic observations favored to constrain the features of this earthquake rupture (Melbourne et al., 1997; Hutton et al., 2001; Hjörleifsdóttir et al., 2018; Cosenza-Muralles et al., 2021a), complementing local and teleseismic datasets (Mendoza & Hartzell, 1995; Courboulex et al., 1997; Pacheco et al., 1997; Escobedo et al., 1998; Hjörleifsdóttir et al., 2018), macroseismic information (Zobin & Ventura-Ramirez, 1998), sea-level measurements (Ortiz et al., 2000), and tsunami surveys (Trejo-Gómez et al., 2015).

The epicenter of the 1995 earthquake (18.864°N, 104.579°W) was ~40 km south of Manzanillo Bay (**Figure 2**). The seismic slip propagated unidirectionally, ~150 km northwest, offshore of Chamela Bay (Ortiz et al., 2000; Hutton et al., 2001; Abbott & Brudzinski, 2015), overlapping entirely the 1932-II earthquake rupture but only a portion of the southern half of the 1932-I earthquake rupture (Azúa et al., 2002; Núñez-Cornú et al., 2016). Coseismic slip on the fault plane occurred at shallow depth (**Figure 2**), coincident with three major asperities (Dominguez Rivas et al., 1997) located offshore of Chamela Bay, where the maximum slip was 4 m, <15 km depth, and offshore Manzanillo and Barra de Navidad where the slip was 1 and 2 m, respectively, both <8 km depth (Mendoza & Hartzell, 1995; Courboulex et al., 1997; Melbourne et al., 1997; Ortiz et al., 2000; Hutton et al., 2001)

GPS instruments recorded subsidence along the coast adjacent to the rupture area (**Figure 2**), with the amount of subsidence reflecting the magnitude of coseismic slip, ranging from 0.06 ± 0.01 m in Manzanillo to the maximum subsidence, 0.21 ± 0.02 m, at Chamela Bay (Hutton et al., 2001). The tide gauge at Manzanillo Harbor also recorded coastal subsidence, inferred from sea-level rise, of 0.11 ± 0.01 m (Ortiz et al., 2000). Additionally, in the central part of the rupture area, a pressure gauge located ~7 km offshore Barra de Navidad recorded coseismic subsidence of 0.40 ± 0.23 m (Ortiz et al., 2000). Two pressure gauges deployed offshore Manzanillo and Barra de Navidad reveal the region of crustal uplift (Ortiz et al., 2000). These observations suggest that the pivot line, which is the surface projection of the down-dip limit of the earthquake rupture (Meltzner et al., 2006; Govers et al., 2017), was entirely offshore.

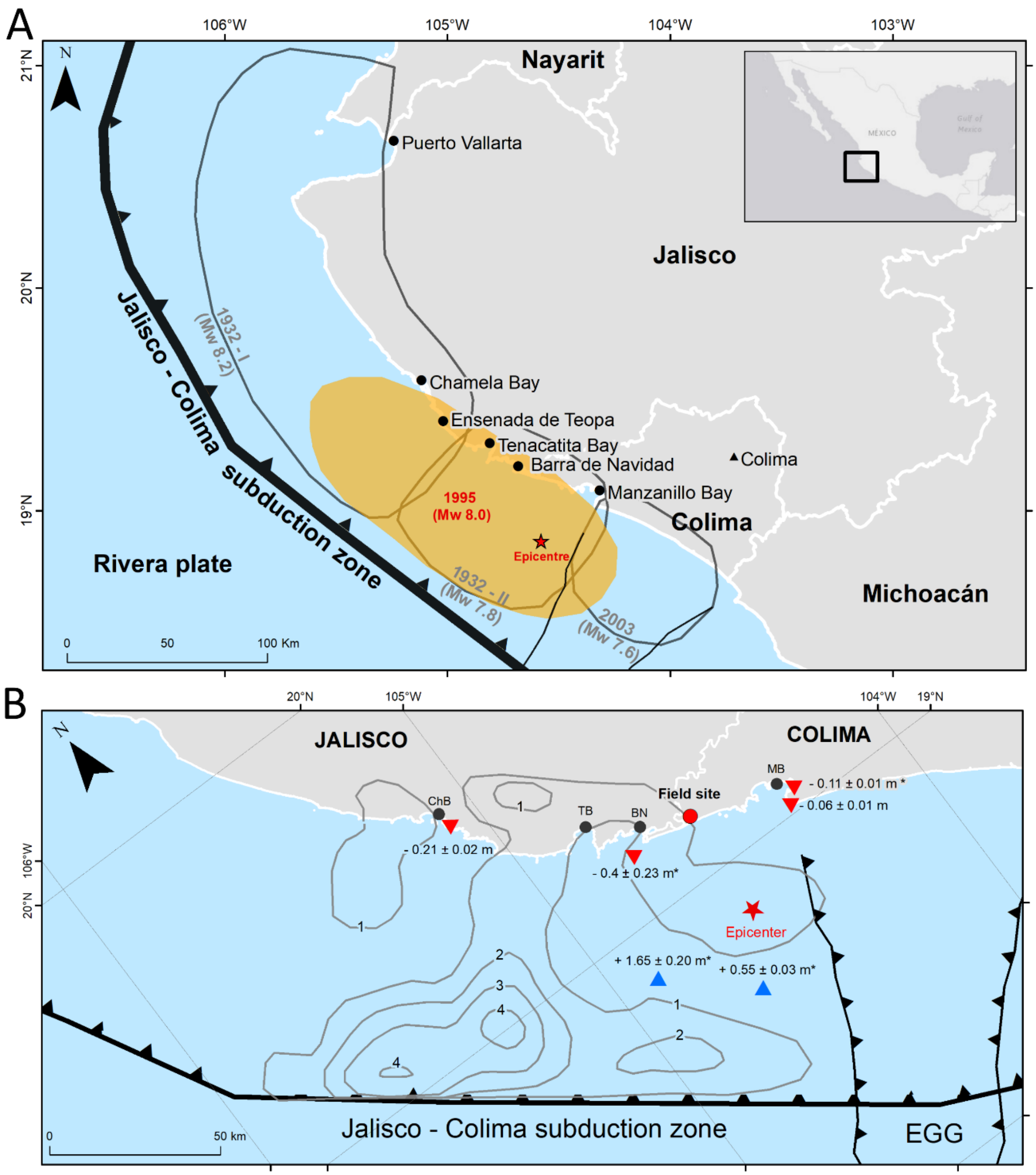

Figure 2. Map of the features of the 1995 M_w 8.0 Colima-Jalisco earthquake. A) Spatial extent of the 1995 earthquake rupture and its relative position along the Jalisco-Colima subduction zone obtained through the distribution of aftershocks (Kostoglodov & Pacheco, 1999). B) Coseismic slip distribution during the 1995 earthquake. Grey contours enclose areas of similar slip and their magnitudes estimated through inversion of teleseismic data (Mendoza & Hartzell, 1995). Blue triangles show the locations of sites that recorded coseismic uplift. Inverted red triangles show the location of instruments that recorded coseismic subsidence. Coseismic deformation values

with * are taken from Ortiz et al. (2000), the rest of the values from Hutton et al. (2001). Coastal towns: ChB = Chamela Bay; TB = Tenacatita Bay; BN: Barra de Navidad; MB: Manzanillo Bay.

2. Regional setting

Our field site, the coastal wetland Estero Potrero Grande, is 55 km north of the 1995 earthquake epicenter, between Barra de Navidad and Manzanillo Bay (**Figure 3**). This site is bracketed by instruments onshore and offshore that recorded coseismic subsidence. Estero Potrero Grande lies on paludal Quaternary sediments in the eastern flank of the deltaic plain of the Marabasco river (**Figure 3**). This wetland is sheltered from wave action by a coastal barrier formed by unconsolidated Holocene littoral deposits. The barrier is up to 500 m wide, comprising a sequence of beach ridges and dune chains, > 5 m above mean sea level (e.g. Méndez Linares et al., 2007; Zuber et al., 2022). This assemblage of Quaternary deposits is surrounded by small to medium hills, 400 – 800 masl, highly incised by fluvial activity (Hernández Santana et al., 1995; Méndez Linares et al., 2007) composed of Granite-Granodiorite, formed during the Mesozoic and early Cenozoic (Rosales Franco & Camargo Soto, 2019).

Estero Potrero Grande is a brackish wetland dominated by the halophyte plant species *Batis maritima* and *Distichlis spicata* (INEGI, 1975). These are two of the species typical along Mexican coasts of the upper intertidal zone and the transition from mangroves to salt pans and salt marshes (Hill et al., 2018; Lonard et al., 2011).

The coast has a semidiurnal and microtidal regime, with the great diurnal range (MHHW - MLLW) 0.73 m (SMN., 2021). These conditions play a vital role in the geomorphology of the wetland, which is composed by narrow and very shallow creek channels (De la Lanza Espino et al., 2013), which progressively damped high and low tides (Zuber et al., 2022). Due to the region is exposed to a strong seasonality with a clear dry and wet season, tidal prism evolves throughout the year in response to interannual estuarine morphodynamics. During the dry season the tidal prism is reduced to its minimum because weak tidal and fluvial fluxes in combination with strong long-shore currents favor the development of an ephemeral sandbar along the river mouth, restricting tidal fluxes and sedimentation. However, during the wet season, June - August, large fluvial discharges breach the mouth of the river, as occurs with most of the coastal wetlands along the

Mexican Pacific (Yáñez-Arancibia et al., 2014). In consequence, the tidal prism reaches its maximum extension, and the wetland turns into a tidal basin, with dominant ebb flow caused by maximum velocities induced by run-off (Lankford, 1977).

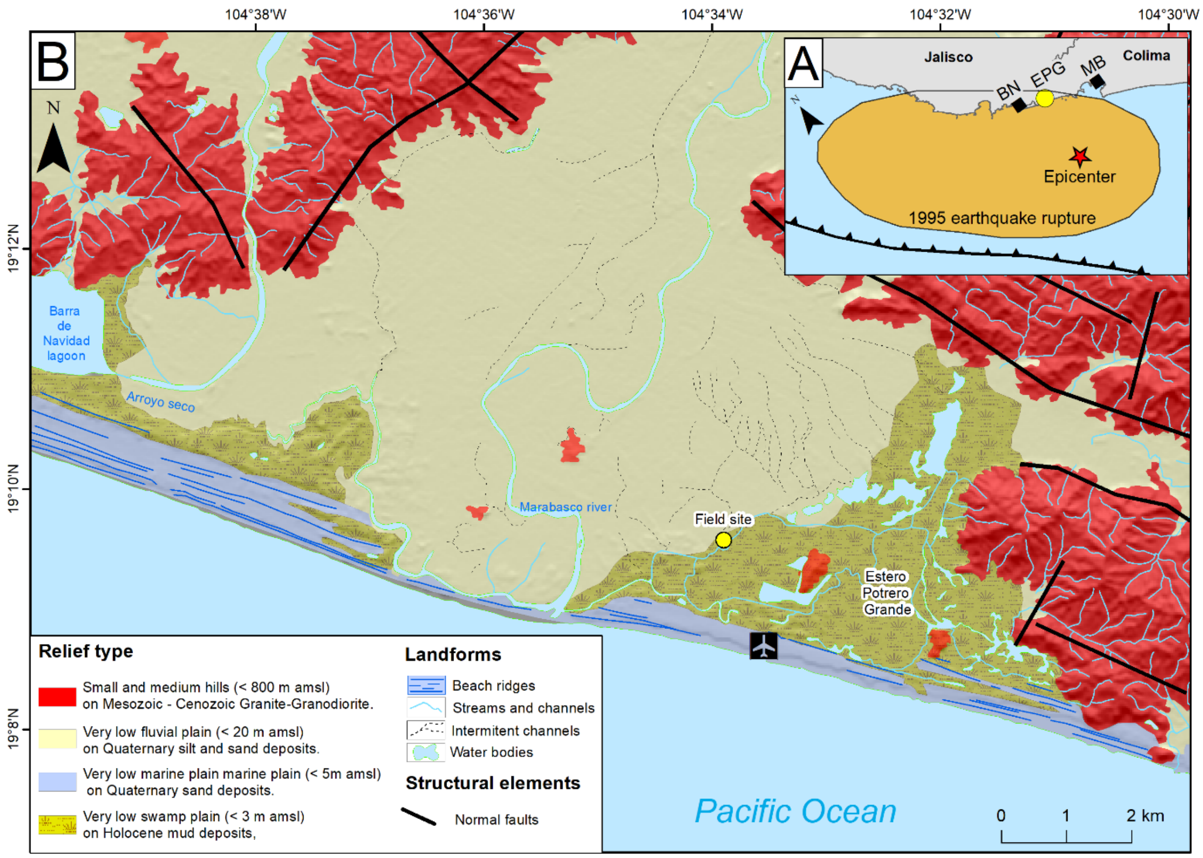

Figure 3. Location of the field site (yellow dot). **A)** Geographic context of the study site. EPG = Estero Potrero Grande, Bn = Barra de Navidad, MB = Manzanillo Bay. **B)** Geomorphological context of the coastal wetland Estero Potrero Grande.

3. Materials and methods.

At numerous locations around the Pacific, the stratigraphic expression of coseismic subsidence in coastal wetlands is revealed by abrupt stratigraphic changes that correspond to a rapid RSL rise. Typically, the lithology comprises organic rich sediments, corresponding to former soils of upper intertidal regions, overlaid by mud, which represents lower intertidal conditions, both units separated by a sharp stratigraphic contact (e.g. Atwater, 1987; Peterson & Darienzo, 1991; Long & Shennan, 1994; Zong et al., 2003; Nelson et al., 2008; Shennan et al., 2013; Briggs et al., 2014; Milker et al., 2016; Kemp et al., 2018; Padgett et al., 2022). As non-tectonic processes can produce similar stratigraphic sequences in tectonically active settings, to corroborate the coseismic origin of organic-mud couplets, a set of criteria was proposed by Nelson et al. (1996): 1) Lateral extent of organic-mud contacts; 2) suddenness of submergence; 3) amount of submergence; 4) tsunami concurrent with submergence; 5) synchroneity of submergence. Although these criteria guide paleoseismic investigations that employ coastal wetland deposits along the temperate coast of North America, earthquake evidence from tropical coastal wetlands have demonstrated their potential to fulfill some of these criteria, despite differences in climate, vegetation, tides and geomorphology (e.g. Dura et al., 2011; Spotila et al., 2015). Hence, we adopt them to investigate the stratigraphy of Estero Potrero Grande and to characterize the signature of the 1995 Colima-Jalisco earthquake.

3.1. Lithostratigraphy.

Sediments from the wetland Estero Potrero Grande were retrieved using a 2.5 cm diameter hand-driven gouge corer. Boreholes were instrumentally levelled with reference to the nearby INEGI geodetic benchmark V0614 (5.0052 m NAVD88). To test the lateral extent of organic-mud contacts, multiple boreholes were analyzed and correlated based on the distinctive characteristics of deposits. To describe the lithology of sediments we adopt the Troels-Smith (1955) scheme. The samples retrieved for laboratory analyses were collected in 50 cm long sections, stored in round PVC tubes, and wrapped in plastic liners.

3.2. Dating and age modelling

Downcore concentrations of ^{137}Cs were measured by gamma spectrometry to establish a chronological control for sediments deposited during the second half of the twentieth century. Chronological markers derived from ^{137}Cs concentrations were interpreted to build a composite age-depth model using two additional ^{14}C ages in the software Bchron (Haslett & Parnell, 2008). The resulting age-depth model allows us to predict the location of the 1995 earthquake in the sediment core.

3.3. Core imaging

To image downcore changes in sediment density at a high resolution, the core material was scanned using the Geotek X-ray computed tomography (X-ray CT scan) imaging system at Durham University. The x-ray was set up at 128.99 kV and 245.7 mA. The vertical resolution is 6 mm (70 pixels) per scanning, with a pixel resolution of 86.87 µm. We produced two orthogonal views of the core section scanned, XZ and YZ views, to visualize the sediments from two different angles using the in-house software (Geotek image viewer). These images were post-processed in the software Image-J (Abràmoff et al., 2004). We initially transformed them into an 8-bit greyscale format to constrain the pixel values of the images within a range of 256 grey intensities. Low intensities correspond to pixel values of 0 (black), which represent sediments with low-densities or high porosity that are commonly associated to highly organic sediments. High intensities are represented by pixel values of 255 (white), corresponding to sediments with high density or low porosity, commonly associated to massive beds of mud and sand. On each image a downcore transect was cast to produce a profile of grey intensity values, following Yan et al. (2021) approach, to qualitatively identify millimetric changes in sediment density.

3.4. Geochemical analysis

To assess the suddenness of submergence, core sediments were scanned at 1 mm resolution with the Geotek Multi-Sensor Core Logger (MSCL-XRF) for identifying salinity change proxies in elemental log-ratios. The Geotek XRF scanner has an X-ray tube with an Rh-anode with a collimator. For light elements (e.g. Al, Ca, Cl, Co, Fe, K, S, Si and Ti), the X-ray voltage was 10 kV and the X-ray current 0.130 mA, while for heavier elements (e.g. Br, Mo, Rb, Sr, Zn and Zr), the settings were 30 kV and 0.500 mA.

3.5. Grain size analysis

Sediment grain size analysis is used to identify any anomalous increases in coarse sediments, to detect the synchronous occurrence of the tsunami accompanying wetland submergence. Bulk sediment pre-treatment follows the HCl + H_2O_2 method in Vaasma (2008). The samples were analyzed using a Beckman Coulter LS 13 320 Laser Diffraction Particle Size Analyzer. The analyzer was set up to average the observations for 90 seconds three times. The outputs are processed through the GRADISTAT extension in MS Excel (Blott & Pye, 2001) to obtain the fraction of sand, silt and clay, and the parameters of grain size distributions (Folk & Ward, 1957).

3.6. Diatom analyses

Fossil diatom assemblages help to assess the suddenness of submergence, identifying paleoenvironmental changes across stratigraphic contacts. Sample preparation followed the standard methods in Zong & Sawai (2015). Diatom counting was conducted through a light microscope with an oil immersion lens at 1,000x magnification. The minimum number of valves counted per sample was 200 (Bate & Newall, 2002). Species identification follows the catalogues of Mexican coastal diatoms (Siqueiros Beltrones et al., 2005; Novelo et al., 2007; López Fuerte et al., 2010; López-Fuerte et al., 2013; López-Fuerte & Siqueiros Beltrones, 2016; Siqueiros-Beltrones et al., 2020). Salinity classes of the species identified are assigned following Denys (1991), Vos & de Wolf (1993), Hartley et al. (1996), Horton et al. (2007), Shennan et al. (2016) and Hocking et al. (2017) Salinity classes correspond to: polyhalobous, which includes marine species; mesohalobous, including brackish species; and oligohalobous, including all freshwater species (Horton & Sawai, 2010; Dura et al., 2016). Final counts are transformed into relative abundance and grouped according to their salinity class (%).

3.7. Quantifying paleoelevations and relative sea-level changes.

Diatom assemblages allow us to quantify the magnitude of any observed wetland submergence, or coastal subsidence. Paleoseismic investigations that employ fossil diatoms to quantify coseismic relative sea/land-level changes rely on the development of diatom-based transfer functions (Hamilton & Shennan, 2005; Shennan & Hamilton, 2010; Garrett et al., 2013; Shennan et al., 2016; Hocking et al., 2017). This approach models statistically the relationship between modern assemblages of species in response to a specific environmental variable (Sachs et al., 1977; Birks, 2005), in this case elevation. The resulting transfer function model is used to calibrate fossil assemblages to estimate paleoelevations (Barlow et al., 2013). The development of a modern training set commonly relies on surface sediments sampled across multiple sites to cover a broad range of environments to have good analogues for the fossil record. To harmonize tidal range in the development of the training set, elevations are normalized and presented as standardized water-level index (SWLI) units (Kemp & Telford, 2015).

Given the limitations we faced in 2020-2021 to carry out fieldwork to build a diatom-based transfer function, paleoelevations from fossil diatom counts are estimated indirectly. Shennan et al. (2016) demonstrated using a fossil record from Alaska, and Hocking et al (2017) in Chile, the relationship between paleoelevations (SWLI), obtained through a diatom-based transfer function, and the cumulative percentage of brackish and marine diatoms (**Figure 4 and Table S.1 in supplementary material**). We create a simple linear regression for each of these datasets (**Figure 4**), using the percentage of marine and brackish species as the independent variable (X), and their corresponding SWLI values, as the dependent variable (Y).

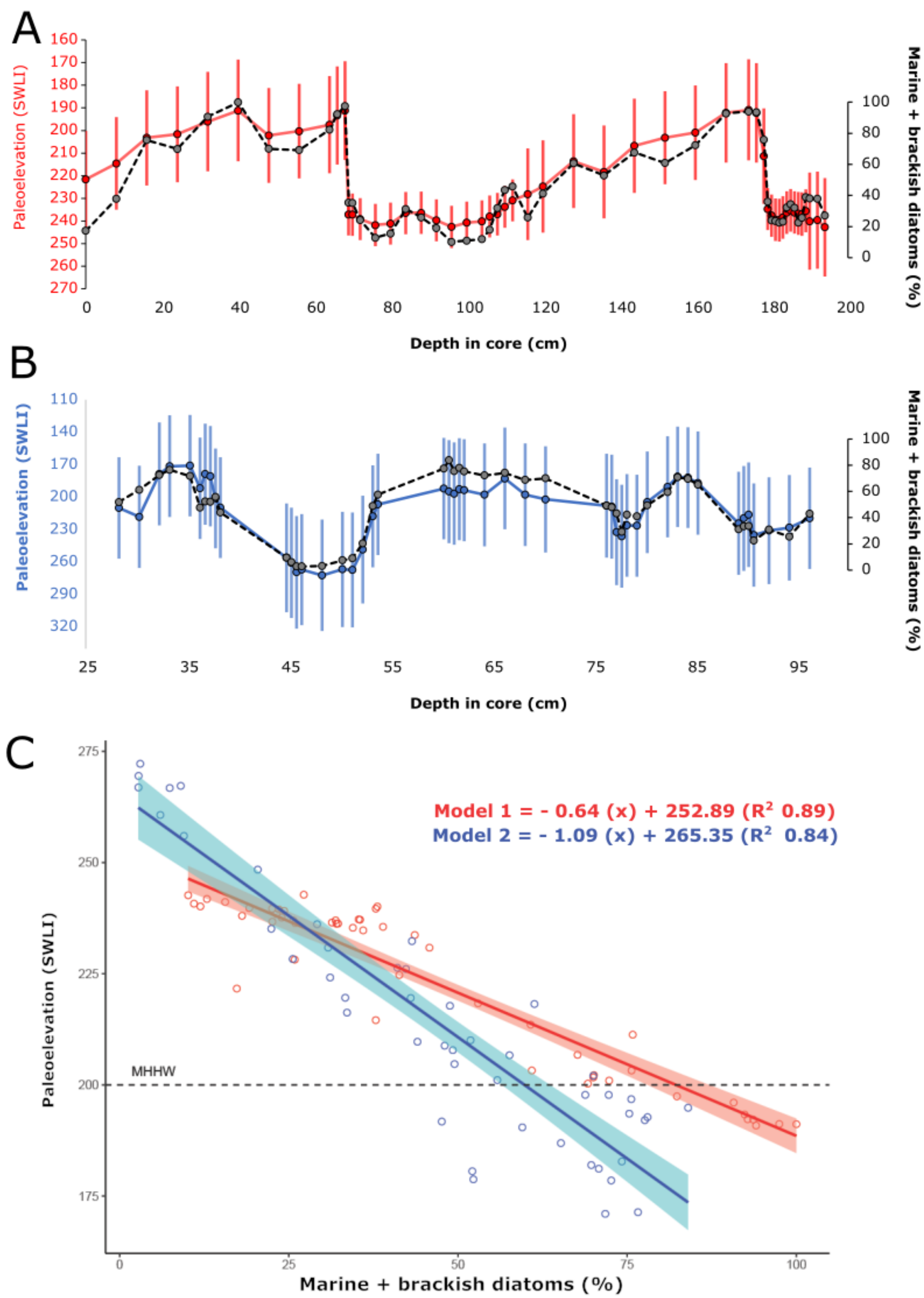

Figure 4. Plots showing the relationship down-core between the percentage of brackish and marine diatoms and paleoelevations (SWLI) derived from quantitative diatom transfer function models. A) Core from Alaska (Shennan et al. 2016); B) Core from Chile (Hocking et al., 2017). C) Linear regression models of the Alaska (Model 1) and Chile dataset (Model 2). The shadow bands bracketing the regression line represent the 95 % confidence interval of each regression line.

We use these linear models, Model 1 (Alaska) and Model 2 (Chile), to estimate the mid-point of paleoelevations, referenced to Mean Higher High Water (m MHHW), using the percentage of brackish and marine diatoms of the fossil counts from Estero Potrero Grande. The output, in SWLI units, is transformed into meters (1 SWLI = 0.003 m) based on the vertical difference between the Mean Higher High Water (MHHW = 200 SWLI) and Mean Tide Level (MTL = 100 SWLI), using the water level datums from the tide gauge at Manzanillo (**Table S.3 in supplementary material**).

The total error (e_T) of our reconstructions is estimated by the square root of the sum of the squares of two individual errors (**Eq. 1**). Error one (e_1) corresponds to the mean of paleoelevation errors of the datasets we use to build the linear regression models (**Table S.1 and Table S.2 in supplementary material**). Error two (e_2) corresponds to the Standard Error of the linear regression:

$$e_T = \sqrt[2]{(e_1)^2 + (e_2)^2} \qquad \textbf{(1)}$$

Following Milker et al. (2016), the magnitude of coseismic subsidence (CS) is estimated using paleoelevation values of the most reliable sample pre-contact (E_{pre}) and post-contact (E_{post}) as:

$$CS = E_{pre} - E_{post} \qquad \textbf{(2)}$$

The error of coseismic subsidence (CS_{error}) is obtained by (**Eq. 3**) the square root of the squared error pre-event (E_{pre}) and the squared error post-event (E_{post}):

$$CS_{error} = \sqrt[2]{(E_{pre}error)^2 + (E_{post}error)^2} \qquad \textbf{(3)}$$

We reconstruct relative sea-level change using the paleoelevation of each sample from the core and the present elevation of each sample calculated as core top minus depth down core. Because we have no precise measure of the relationship between NAVD88 and tide levels in the wetland, rather than the tide gauge at the coast, we show RSL for each sample as relative to zero at present:

$$RSL_{sample} = Elevation_{sample} - Paleoelevation_{sample} \quad \textbf{(4)}$$

4. Results

4.1. Stratigraphy

Eleven boreholes were manually drilled in an area adjacent to a creek channel that cut the paludal plain in a NE-SW direction (**Figure 5**). The cores are 1.3 to 2.2 km from the shoreline; and the distance to the mouth of the Marabasco river is 2.6 to 3.6 km. Among this set of cores, five show a coherent stratigraphy, allowing us to correlate the stratigraphic units identified in the field. The stratigraphy of the site consists of a basal sand bed with rare fragments of angular and rounded gravel, smaller than 5 cm in diameter. Above this basal unit we identify four horizontal beds of organic silt, interrupted by silt, forming four abrupt stratigraphic contacts (A to D). We focus on contact A, which is the shallowest stratigraphic contact that represents the most recent event imprinted in the stratigraphy of Estero Potrero Grande.

We mapped contact A for over 1 km, as far as 2 km inland, always in sites adjacent to the creek channel. In core MAR001 (19.158°N, 104.567°W), contact A is at 25 cm depth, consisting of a dark brown-grey silty clay with humified organic matter overlaid abruptly by grey silt with occasional roots. Approximately 380 m northeast, at MAR004 (19.159°N, 104.564°W), the underlying unit is composed of brown organic silt overlaid abruptly, at 23 cm depth, by a grey mud lens. At MAR005 (19.160°N, -104.564°W), stratigraphic contact A occurs at 28 cm, where a bed of grey silt abruptly replaces a horizontal bed of black organic silt with highly humified herbaceous remains. At MAR010 (19.163°N,104.560°W) and MAR009 (19.163°N,104.56°W), the contact is at 21.5 cm and 26 cm depth, respectively, and shows an underlying black organic silt bed overlaid by grey silt.

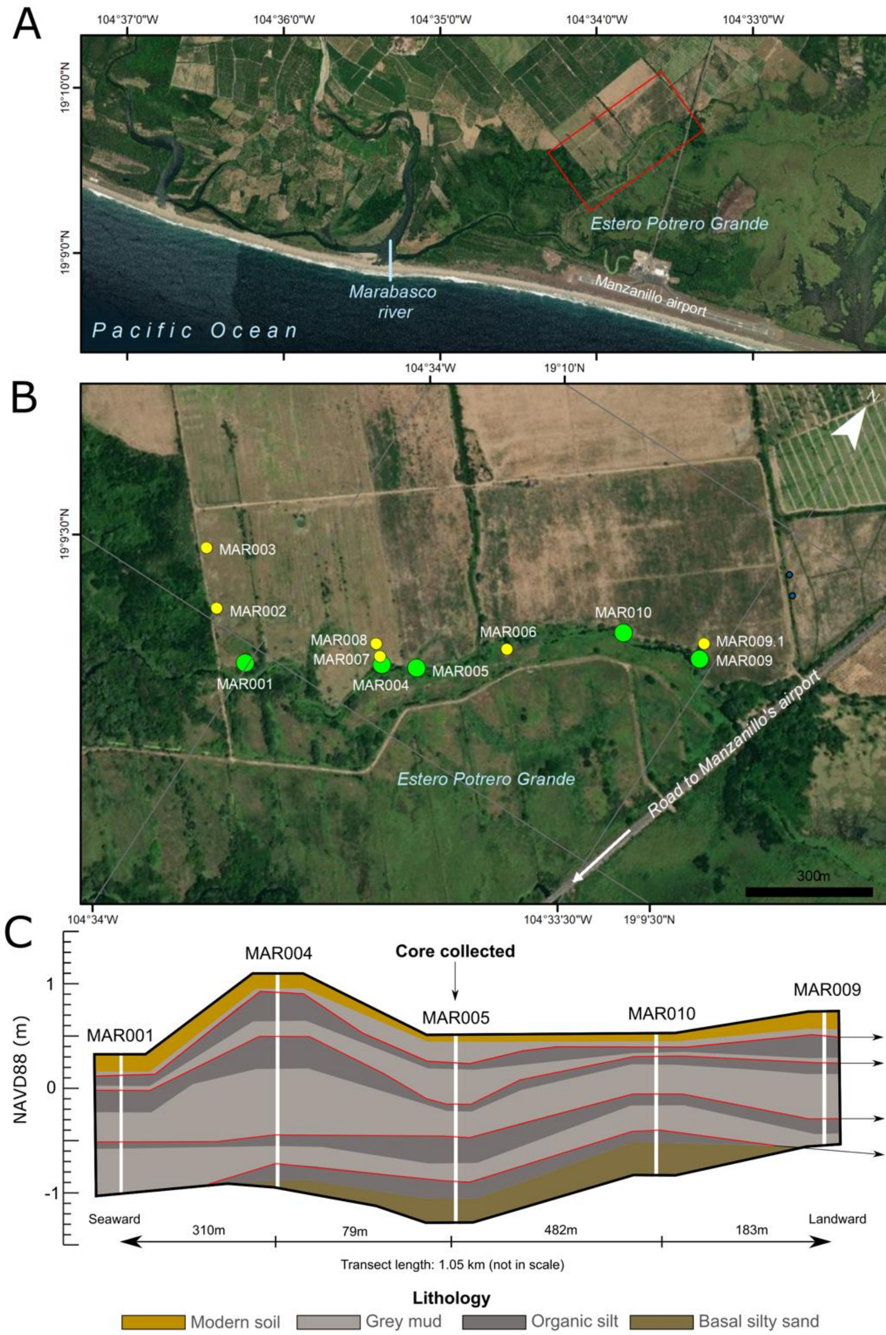

Figure 5. Shallow stratigraphy of the study site in Estero Potrero Grande. **A)** Aerial image of Marabasco river coastal plain showing location of study site (red inset box). **B**) Location of exploratory boreholes. Those shown in yellow contain stratigraphic changes that could not be correlated across the site. Green dots indicate the location of cores summarized in the stratigraphic diagram. **C**) Stratigraphic correlations of coring sites. The four abrupt stratigraphic contacts, A to D, are indicated with the red lines. Stratigraphic contact A is investigated in this study. Source of the base map, ESRI ArcMap.

The stratigraphic sequence across contact A is displayed at a high resolution in **Figure 6**. The CT scan images demonstrate that the organic unit below contact A contains pixels with relatively low intensity values, which on average are below 125. These pixel values clearly contrast with those within the grey mud unit above the stratigraphic contact, with intensities between 150 and 200. The CT scan images reveal that the transition between these units is marked by a sharp increase of gray intensities, as pixel values rise to > 200. This bed of high intensity values is 1mm thick, showing a sharp basal contact and a high abundance of coarser sediments, which are represented by white mottles < 1mm long (**Figure 6 B**). Overlying this unit of coarser sediments, the CT scan images reveal the presence of a homogeneous bed with high density, resembling a cohesive mud cap.

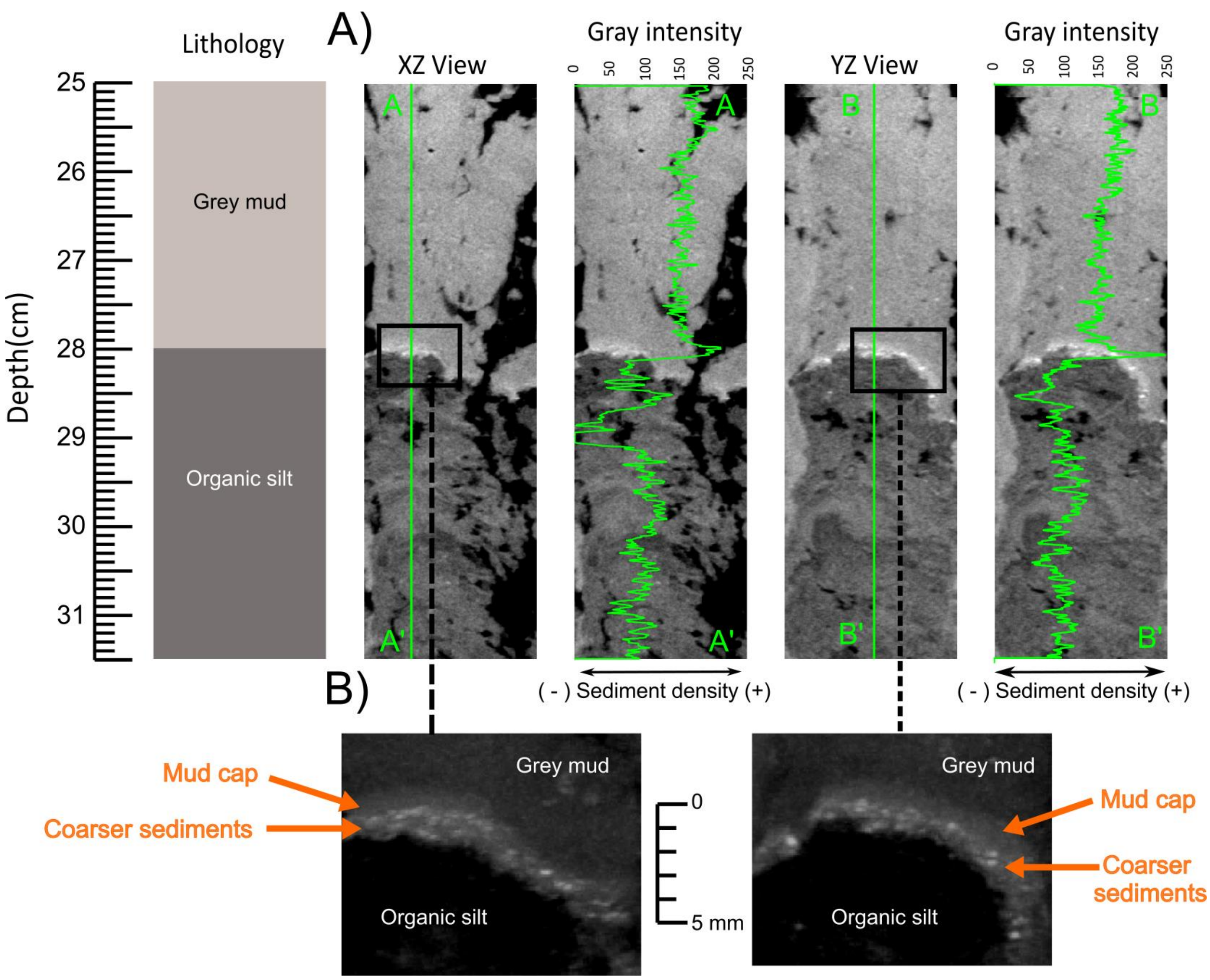

Figure 6. High-resolution CT scan images of stratigraphic contact A at two orthogonal views (XZ and YZ). **A)** Line graphs (green) over the images indicate changes in pixel gray intensities

downcore of the transects A-A' and B-B' respectively. **B)** CT scan images in high contrast show the structure of the thin bed (1 mm) of coarse sediments overlaid by a layer of cohesive mud.

4.2. Sediment chronology

Downcore concentrations of ^{137}Cs fluctuate between 0 and 1.78 mBq g^{-1}, within the depth range 0 - 104 cm in core MAR005 (**Figure 7**). The first chronohorizon to identify using the ^{137}Cs profile corresponds to the onset of measurable ^{137}Cs in sediments, which represents the initial incorporation of ^{137}Cs in surface deposits (1952 ± 2 CE), when measurable global fallout initiated (Corbett & Walsh, 2015; Drexler et al., 2018). In our profile, measurable ^{137}Cs starts at 88 ± 4 cm. Although concentrations at this depth clearly depart from zero values, it is only at 80 ± 2 cm where concentrations exceed the detection limit. Based on these features, we can only argue that the ^{137}Cs onset is constrained within the depth range 78 - 92 cm, which includes the thickness of the measured samples. A second chronohorizon corresponds to the year (1963 ± 1 CE) of maximum fallout (Corbett & Walsh, 2015; Drexler et al., 2018). The first peak in concentrations occurs at 72 ± 2 cm, but the most prominent peak of concentrations occurs at 67 ± 1 cm (1.79 mBq g^{-1}). We therefore establish the ^{137}Cs spike to be between 66 and 74 cm.

Two samples, at 67 and 99 cm, were ^{14}C dated, showing an excess of modern carbon fraction. Using the latest post-bomb curve NHZ2 (Hua et al., 2021), their calibrated age ranges result in two probability distributions. At 67 cm, the age ranges are 1961 – 1962 CE (13.7%) and 1980 – 1983 CE (86.3%). At 99 cm the age ranges are 1954 – 1956 CE (38.5%) and 2016 – 2019 CE (61.5%). Based on their stratigraphic position, their more likely age ranges of these samples are 1961 – 1962 CE and 1954 – 1956 CE, respectively. Our composite age-depth model results in a mean rate of sediment accumulation of 1.28 ± 0.01 cm yr^{-1} in the last ~68 years. The modelled age range of the stratigraphic contact A is 1985 – 2003 CE (1σ), with a mean age of 1995 CE.

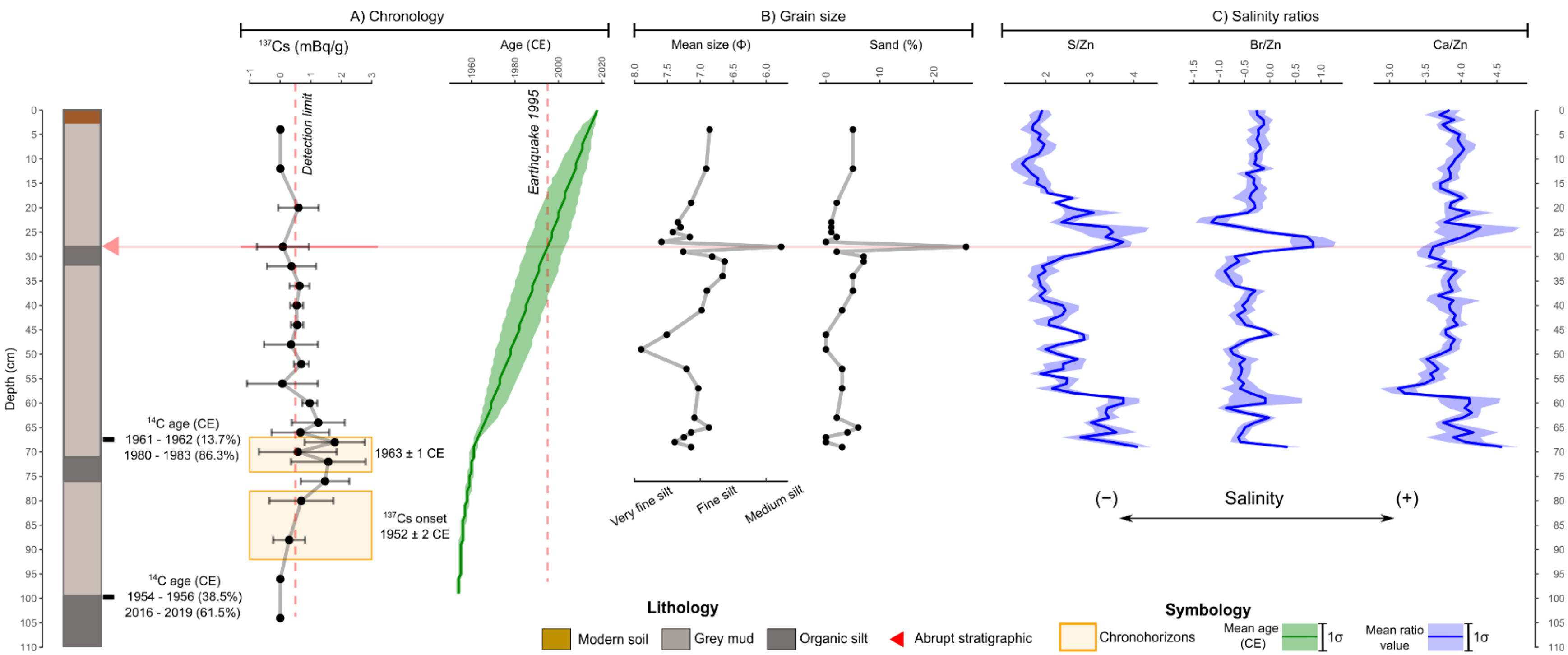

Figure 7. **A)** Chronological control to constrain the age of the stratigraphic contact A. The interpolated age-depth model resolution is 2 cm **B)** Downcore changes of grain size **C)** Element log-ratios to reveal changes in salinity.

4.3. Grain size analysis

Measurements of mean grain size below the stratigraphic contact do not show significant variability (**Figure 7**). From 70 to 29 cm depth sediments are classified as fine to very fine silt (mean 8 - 6 φ) with very low percentage of sand (<7%). At 28 cm depth, there is an abrupt increase in sand fraction (26%), and the sediments are classified as medium silt (mean = 5.77 φ). This anomalous bed of coarse sediment is less than 0.5 cm thick, and it was not visible to the naked eye. Above 28 cm depth, the percentage of sand decreases abruptly (~0%) and the mean size of sediment returns to fine silt.

4.4. Geochemistry and salinity changes

Three elemental log-ratios are calculated using Sulphur (S) Bromine (Br) and Calcium (Ca), as they are indicative of marine incursions in coastal wetlands of the Mexican Pacific, associated to either gradual (e.g. Figueroa-Rangel et al., 2016) or abrupt relative sea-level changes caused by tectonic (e.g. Ramirez-Herrera et al., 2007; Ramírez-Herrera et al., 2012, 2014) and hydrometeorological events (e.g. Bianchette et al., 2016, 2017). These elements were normalized using the terrestrial element Zinc (Zn), which is highly abundant in fluvial sediments of the Mexican Pacific coast, including the Marabasco river (Marmolejo-Rodríguez et al., 2007; Martinez et al., 2014). High values of these three ratios indicate a higher influence of marine waters in the wetland, whereas low ratios suggest a decrease in marine influence, or a terrestrial input driven by fluvial sedimentation.

Below stratigraphic contact A, from 50 cm upwards, these three ratios do not show significant fluctuations (S/Zn from 1.4 to 31, Ca/Zn from 3.4 to 4.9, Br/Zn from -1.2 to 0.2) (**Figure 7**). Around 30 cm, S/Zn and Br/Zn depart from their background values to reach a significant peak at 28 cm (S/Zn = 3.9, Br/Zn = 1.8) and 26 cm (Ca/Zn = >4.0), the largest change in the 70 cm long core. Roughly, rom 20 cm to the top of the core, the three ratios approximate to their background values, as those underlying contact A.

4.5. Biostratigraphy and paleoelevations.

Fossil diatom assemblages from the record of Estero Potrero Grande show a mix of freshwater (44 – 95%), brackish (4 – 23%) and marine (1 – 36%) taxa (**Figure 8**). Between 57 to 34 cm depth freshwater diatoms dominate the assemblages, reaching up to 90% of the assemblages. The dominant species are *Luticola mutica* (> 30%) and *Diadesmis confervaceae* (> 50%). Within the 3 cm below the stratigraphic contact (29 - 32 cm), there is an increase of *Halamphora submontana* (5 – 17%). Above the stratigraphic contact, at 28 cm depth, there is a spike of *C. meneghiniana* (> 15%). At 27 cm depth, 1 cm above contact A, there is an abrupt increase in marine and brackish species (55 %), with *Nitzschia grossestriata* (18%) and *Paralia sulcata* (11%) the dominant species that reflect this change. Four centimeters above the stratigraphic contact, from 24 cm depth to the top of the core, diatoms show a gradual increase in freshwater diatoms (> 70%), with *L. muticola, D. confervacea, G. affine* and *H. submontana* the most abundant species.

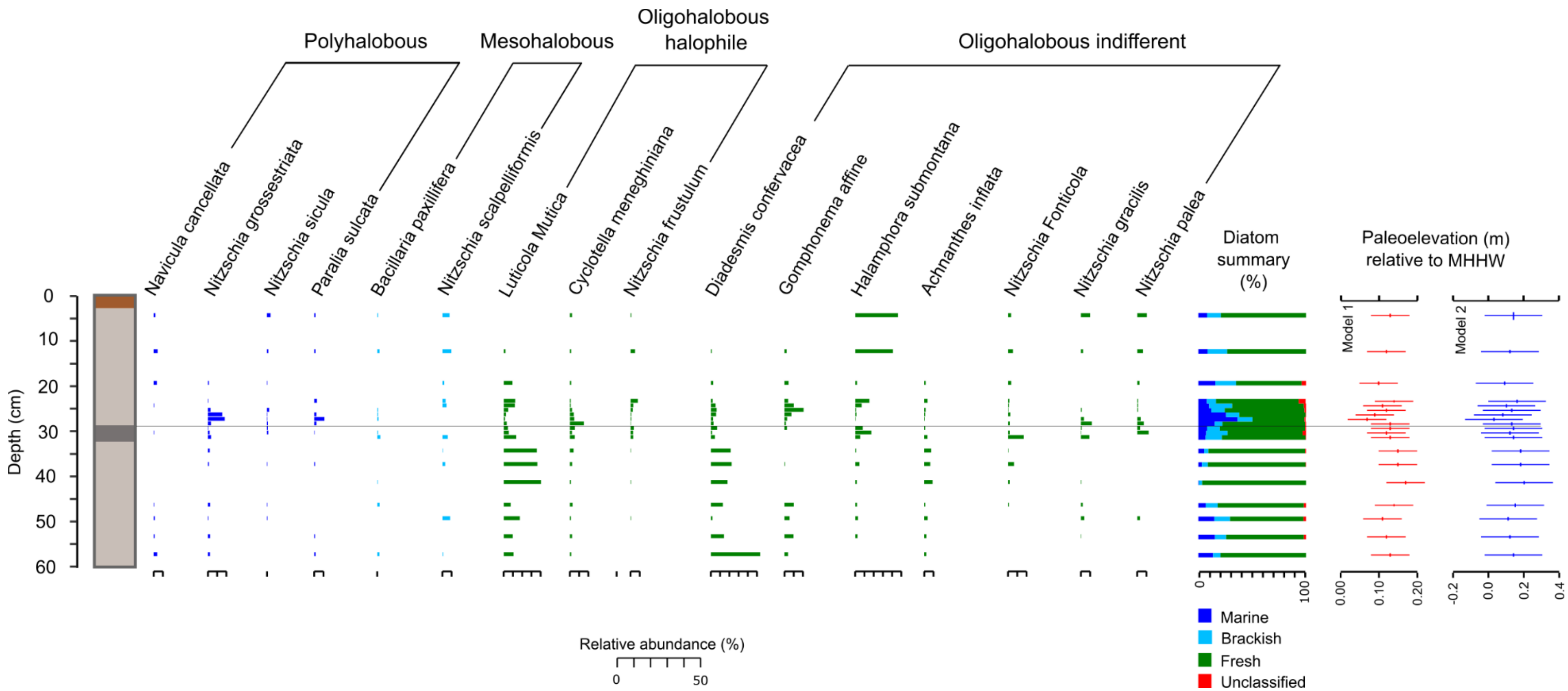

Figure 8. Diatom biostratigraphy and paleoelevations of core MAR005. Plotted are diatom species >5% that appear in at least five samples.

Paleoelevation reconstructions (**Figure 8**) beneath the organic unit underlying contact A, reach maximum values, ~0.14 m MHHW with fluctuations < 0.02 m. Within the organic unit beneath the contact, paleoelevations are 0.12 ± 0.05 m MHHW, predicted by Model 1, and 0.12 ± 0. 16 m MHHW predicted by Model 2. Paleoelevation changes within the 5 cm thick organic unit are negligible (<0.01 m). Above the stratigraphic contact, at the bottom of the overlying silty bed (28 cm), our models do not show any change in paleoelevation. It is at 27 cm depth, where paleoelevation estimations change abruptly, from 0.13 ± 0.05 m MHHW to 0.7 ± 0.05 m MHHW (Model 1), and from 0.14 ± 0.16 m MHHW to 0.03 ± 0.16 m MHHW (Model 2). This is a vertical land-level change of -0.06 ± 0.08 m (Model 1) and -0.11 ± 0.23 m (Model 2) (**Figure 9**).

The abrupt change of paleoelevation at 27 cm gradually increases up in the core. Our reconstructions indicate that at 23 cm, paleoelevations values are similar to those found within the organic unit below the stratigraphic contact A. At this dept Model 1 is 0.14 ± 0.05 m MHHW, and Model 2 0.16 ± 0.16 m MHHW. It is worth noting that this change in paleoelevations is gradual but steady within this depth range. Toward the top of the core, paleoelevations remain stable with changes <0.03 m.

Our long-term RSL reconstructions show an overall positive trend (**Figure 9**). RSL altitude increases from -0.55 ± 0.05 m to -0.02 ± 0.05 m (Model 1) and from -0.56 ± 0.16 m to -0.03 ± 0.16 m (Model 2) between 1972-2018 CE. The total RSL change over this period is +0.53 m, resulting in a linear change rate of 1.32 ± 0.02 cm yr^{-1}. These reconstructions allow us to identify four periods of RSL change: 1) from 1972 CE to 1994 CE, RSL is gradually rising; 2) In 1995 CE, there is an abrupt RSL rise; 3) from 1995 CE to 1999 CE, RSL begins to fall gradually; 4) and from 1999 to 2014, RSL is gradually rising.

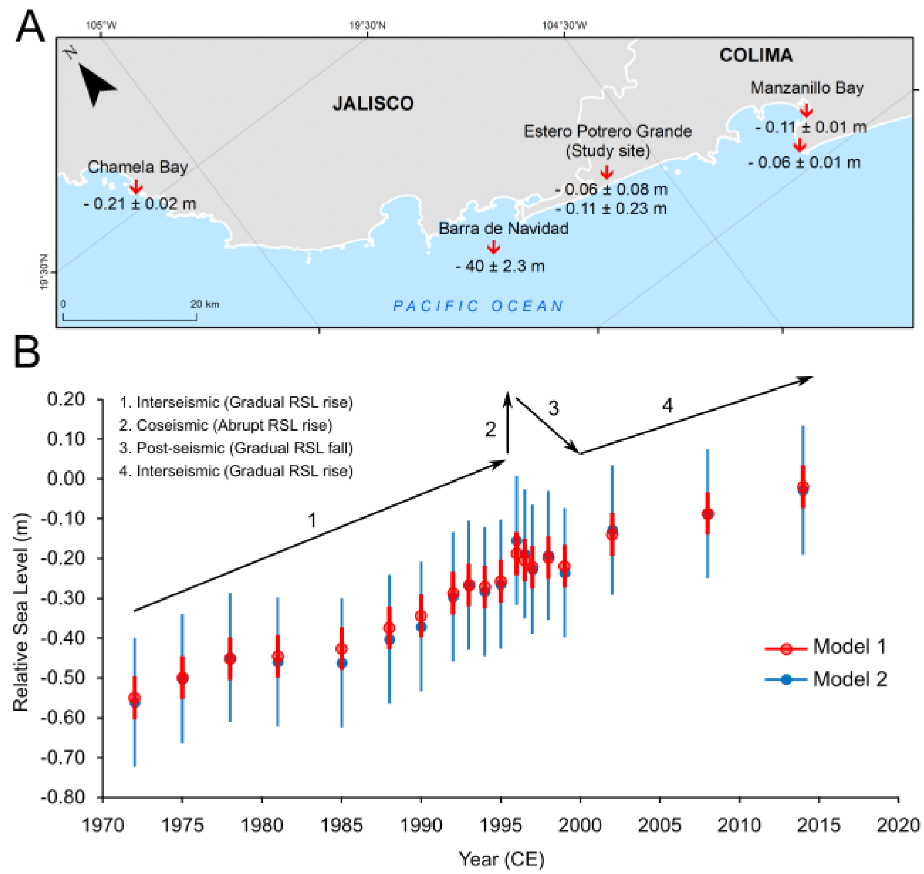

Figure 9. Magnitudes of coseismic subsidence along-strike and RSL changes (1972-2014) recorded at Estero Potrero Grande. **A)** Map showing the spatial coherence between instrumental measurements and our estimations of subsidence caused by the 1995 earthquake. **B)** Relative sea-level changes reconstructions before, during and after the 1995 earthquake, showing the stages of the earthquake deformation cycle as the most probable mechanisms to explain the RSL trends.

5. Discussion.

The stratigraphy beneath the coastal wetland Estero Potrero Grande shows a sequence of four minerogenic beds abruptly overlying organic rich sediments. These stratigraphic sequences are similar to the sedimentary signature of multiple episodes of coastal wetland submergence produced by megathrust earthquakes elsewhere (Atwater, 1987; Nelson et al., 1996; Shennan et al., 1998; Dura et al., 2011). The shallowest event, contact A, is the latest event imprinted in the local stratigraphy that more likely reflects the episode of coastal subsidence in this site during the 1995 Colima-Jalisco earthquake (Mw 8).

5.1. Estero Potrero Grande preserves an extreme event that occurred in 1995 CE.

Our composite age-depth model, including ^{14}C ages and ^{137}Cs based chronohorizons, confirm that contact A was produced within the last 55 years under a relative steady rate of sediment accumulation (1.28 ± 0.01 cm yr^{-1}) at least four times higher than the rate estimated in other tidal mudflats of the Mexican Pacific coast (Ruiz-Fernández & Hillaire-Marcel, 2009) and at least one order of magnitude higher than rates estimated in coastal lagoons of the Atlantic and Pacific margins of Mexico (Ruiz-Fernández & Hillaire-Marcel, 2009; Cordero-Oviedo et al., 2019). The rate of sediment accumulation at our field site approaches rates estimated in fluvial settings of the Mexican Pacific (e.g. Ruiz-Fernández et al., 2002). Our chronology indicates the high influence of the Marabasco river, promoting the vertical aggradation of this wetland and the rapid burial of the land surface. The modelled age range of contact A (1985-2003 CE) not only brackets the year of the Colima-Jalisco earthquake, but it shows a mean age (1995 CE) centered on the year of this event.

5.2. Testing the coseismic origin of contact A (1995 CE).

To confirm, or rule out, the coseismic origin of contact A (1995 CE), we discuss the properties of the sediments bracketing this contact based on the following paleoseismic criteria of Nelson et al. (1996): 1) lateral extent of contact A, 2) abruptness of wetland submergence, 3) amount of submergence and 4) tsunami evidence concurrent with submergence.

5.2.1. Mapping the lateral extent of Contact A.

Our field data provides evidence to determine the lateral extent of contact A. To correlate this stratigraphic contact along the coring transect we consider the distinctive characteristics of the lithofacies bracketing the stratigraphic contact, their depths and their stratigraphic position (Nelson et al., 1998). The underlying organic unit shows very similar characteristics in all cores. It is a highly humified horizontal bed of organic silt, ~5 cm thick, with occasional remains of plants. In all cores this unit is clearly differentiated from the overlying sediments in the field instrumental measurements by a sharp contact between organic silt to silt up core. Contact A is constrained within the range 21 - 28 cm below the land surface across the field site.

Our field observations confirm that only those sites adjacent to the creeks record the stratigraphic contact A. If this contact reflects coastal subsidence during the 1995 earthquake, the small amount of subsidence, in the order of 0.1 m, will likely limit the spatial extent of the area to cross the threshold from one type of sedimentary environment to another, i.e. a creation threshold (e.g. Nelson et al., 2006), as observed in marshes affected by the 2016 Mw 7.6 Chiloé earthquake (Brader et al., 2021). Additionally, the microtidal regime limits those areas regularly inundated by tides to narrow bands adjacent to the creek channels and the channels themselves. Proximity to creeks, as a source of sediment, also improves the potential of these sites to record tsunami sedimentation (e.g. Atwater, 1987, 1992; Morton et al., 2011).

The shallow stratigraphy of this wetland demonstrates that within a period of 55 years, only one event produced a significant stratigraphic change. Consequently, the mechanism of creation of contact A had to be an exceptionally large event capable of changing the dominant sedimentation pattern and burying the land surface over a 1 km distance in 1995 CE.

5.2.2. Evidence of sudden wetland submergence

The salinity ratios S/Zn, Br/Zn and Ca/Zn are our first line of evidence to demonstrate wetland submergence. Immediately above the contact, the Br/Zn ratio shows a clear peak. The ratio decreases abruptly a couple of centimeters above contact A. The S/Zn ratio reaches its maximum values slightly above contact A. This ratio not only peaks above the contact but it remains relatively high, suggesting a long-lasting change in salinity conditions. The ratio Ca/Zn shows a more gradual increase above contact A, with a smaller magnitude of change compared to values elsewhere in the core. Although these ratios, overall, show a similar trend across contact A, their discrepancies can be explained by the response of the wetland during the creation of contact A.

Because Sulphur is hosted in marine plants and Bromine is associated with marine organic carbon content (Rothwell & Croudace, 2015), their abrupt increase above contact A most likely reflects the rapid penetration of marine waters during the initial stage of wetland submergence in 1995 CE. Bromine and Sulphur have proved to be indicative of marine incursions in other coastal settings (Chagué-Goff et al., 2017), including the Mexican Pacific coast (Roy et al., 2012). The long-lasting concentrations of S/Zn, and the rapid depletion of Br/Zn, is explained by the higher abundance of Sulphur in the waters of the Mexican Pacific (Padilla et al., 2007). The slow and constant increase of Ca/Zn above the contact, more likely represents the gradual establishment of the new marine influenced environment above contact A, considering that Calcium is a major element linked to marine organisms, calcium carbonate shells and marine biogenic content (Rothwell & Croudace, 2015).

Diatom assemblages are the second line of evidence to confirm wetland submergence. Below contact A, the species *D. confervaceae* and *H. submontana* indicate that this environment was similar to the modern wetland conditions. These species dominate in shallow lentic freshwater systems (Szabó et al., 2004; Vélez et al., 2006; Lezilda Carvalho Torgan & Cristiane Bahi Dos Santos, 2008; Jaramillo et al., 2021), fluvially dominated (Compère, 1984; Qingmin et al., 2015; Cocquyt et al., 2019). The first centimeter above the stratigraphic contact shows a spike of *C. meneghiniana*, which is a planktonic freshwater to brackish species (Denys, 1991). This spike indicates an increase in salinity conditions, as this species lives in estuarine environments (Zong et al., 2006). *C. meneghiniana* might represent the sequential transition to an environment dominated by marine taxa. However, as its spike is concurrent with the abrupt increase of sand, we cannot rule out the hypothesis that *C. meneghiniana* is the signature of the tsunami that accompanied the 1995 CE earthquake.

One centimeter above the stratigraphic contact, at 27 cm, the abrupt increase in the marine species *P. sulcata* and N. *grossestriata* confirm wetland submergence. *P. sulcata* is a planktonic species indicative of a high influence of marine conditions in brackish and freshwater environments (Vos & de Wolf, 1993; Zong, 1997; McQuoid & Hobson, 1998; McQuoid & Nordberg, 2003). The species *N. grossestriata* dominates mangroves and shallow subtidal environments in coastal wetlands of Baja California (e.g. Martínez-López, 2004; Siqueiros-

Beltrones et al., 2017). These species suggest that sediment accumulation above contact A occurred around MHHW.

Wetland submergence seems to be reversed gradually during the following four to five years after the creation of contact A. This is confirmed by the return of salinity ratios to their background values and the increase of supratidal diatom species, specifically *H. submontana* and *L. muticula*. This pattern of wetland emergence post-1995 CE is steady and the mechanisms that can explain these changes in salinity and diatom assemblages are described in the following section.

5.2.3. Coseismic subsidence and relative sea-level changes.

We estimate coseismic marsh submergence across contact A as 0.06 ± 0.08 m (Model 1) and 0.11 ± 0.23 m (Model 2), based on the differences in paleoelevation between the samples from 29 and 27 cm core depth as the spike of sand at 28 cm may distort the estimates (**Figure 8**). This elevation change is equivalent to 9% and 15% of the great diurnal tidal range, respectively. These submergence estimates agree with coseismic subsidence values at the coast recorded by geodetic instruments and show a spatial coherence (**Figure 9**) with the pattern of subsidence and uplift discussed previously (**Section 1.2**), broadly reflecting the along-strike variations of coseismic slip (**Figure 2**). For example, at Manzanillo Bay, ~ 30 km southeast from our study site, a GPS station records 0.06 ± 0.07 m subsidence, with maximum slip offshore estimated ~1m (Mendoza & Hartzell, 1995), and at Chamela Bay, ~70 km northwest, coseismic slip peaks at ~4 m, the magnitude of subsidence was 0.21 ± 0.01 m (Hutton et al., 2001).

Our RSL reconstructions, based on the paleoelevation estimates from the core, show an overall positive trend of +0.53 m in 42 years (1972 - 2014 CE) (**Figure 9**). Numerous factors contribute to RSL change, including global mean sea level, regional modifications to the global value due to factors such as ENSO, deltaic subsidence caused by sediment loading from the prograding floodplain and delta of the Marabasco river, compaction of unconsolidated wetland sediments, as well as vertical crustal motions during subduction earthquake cycles. We suggest that the deviation seen from the overall RSL trend 1972 – 2018 CE reflects the different stages of the latest earthquake cycle.

The RSL reconstructions show rapid rise caused by coseismic subsidence in 1995 CE, followed by a short period of RSL fall. This is consistent with post-seismic uplift outpacing the non-seismic components contributing to RSL change. GPS records show that the coast adjacent to the earthquake rupture uplifted rapidly during the first 4-5 years after the earthquake (Hutton et al., 2001; Cosenza-Muralles et al., 2021a). This pattern of deformation is partially explained by after-slip deformation, which represents the behavior of the fault areas around the rupture zone over time scales ranging from of a few months to a few years after the seismic event (Wang et al., 2012). The area of afterslip was identified 10-20 km farther downdip of the earthquake rupture, extending all the way down beneath the coast, inducing the pattern of uplift observed along the coast adjacent to the rupture (Cosenza-Muralles et al., 2021a). A second process that can explain coastal uplift is viscoelastic rebound, or transient fluid flow in the upper crust, a process that could occur largely during the first few years after the earthquake (Hutton et al., 2001).

By 1999-2000 CE, the trend of RSL fall reverses to RSL rise as identified earlier (**Figure 9**). Between Manzanillo and Barra de Navidad, geodetic instruments demonstrate that the coast between these years began to experience subsidence at a rate of ~3 mm yr^{-1} (Cosenza-Muralles et al., 2021b). This quick reversal of land-level change is not unlikely as it has been observed in earthquakes of similar magnitudes elsewhere (Wang et al., 2012). Geophysical models suggest that this trend of coastal subsidence is partially explained by the strong locking of the plate interface, extending to a depth of up to 40 km (Cosenza-Muralles et al., 2021b). However, it is important to highlight that the local rate of sea-level rise, 2.6 ± 0.9 mm yr^{-1} at Manzanillo Bay (Buenfil-López et al., 2012), and the rate of land subsidence, induced by the rapid accumulation of sediments in this wetland (1.28 ± 0.01 cm yr^{-1}), also contribute to accelerate or reverse the RSL trends across the different stages of the earthquake deformation cycle at this site.

5.2.4. Wetland submergence concurrent with a high-energy event deposition.

The last criterion corresponds to tsunami evidence accompanying subsidence. Anomalous layers of coarse sediments, composed mainly by sand, deposited in low-energy coastal settings are widely used to infer past tsunamis and earthquakes in tectonically active coasts. In Estero Potrero Grande, our field evidence does not reveal visible evidence of sand deposition associated to contact A. However, our laboratory results show the presence of a thin (< 1 mm) layer of sandy sediments that overlies sharply the organic silt unit (**Figure 6**) and clearly contrast with the background sedimentation (**Figure 7.B**). This minimum evidence suggests the occurrence of a high-energy event, which is concurrent with a rapid increase of salinity conditions, represented by the spike of the ratios Br/Zn and S/Zn and the high abundance of *C. meneghiniana,* which likely represents the displacement of estuarine waters to the coring site.

A post-event survey indicates that the 1995 tsunami run-up at this location was ~4 m, flooding the beach of the coastal barrier that protects the wetland, with no evidence of beach barrier overtopping (Borerro et al., 1997). Hence, if this millimetric sand deposit is the signature of the 1995 tsunami, these coarse sediments would only have reached the back-barrier wetland as the tsunami wave breached the river mouth and flooding only those low-lying areas adjacent to creek channels. Numerical models demonstrate that in similar settings along the Mexican Pacific, tsunamis of similar heights can penetrate as far as at 1 km inland through river and creek channels (e.g. Sanchez & Farreras, 1987; Farreras et al., 2007; Corona & Ramírez-Herrera, 2012). Under this scenario, when the 1995 CE tsunami reached the coring site, which is more than 1 km from the shoreline, the complex network of meandering channels and the presence of dense mangrove vegetation would have caused it to lose energy, reducing its capacity to carry coarse sediments and deposit them inland. Indeed, the presence of a millimetric mud cap (**Figure 6**) indicates settling of suspended material due to a decline of flow velocity (Kelsey et al., 2005; Wilson et al., 2014; Chagué-Goff et al., 2015). Sand deposits of similar thickness (< 1 cm) occur frequently at the landward limit of tsunami deposits elsewhere (e.g. Moore et al., 2006; Paris et al., 2007; Takashimizu et al., 2012; Garrett et al., 2013; Chagué-Goff et al., 2015; DePaolis et al., 2021), showing sedimentary features similar to those found in Estero Potrero Grande (e.g. Atwater et al., 1995; Morton et al., 2011; Chagué et al., 2018).

The physical, chemical and micropaleontological properties of the millimetric sand layer at contact A and its synchroneity with abrupt wetland submergence suggests that this deposit is more likely the signature of the tsunami that followed the 1995 CE earthquake. We argue that our coring sites are sensitive to record the occurrence of unusual high-energy waves that affect the Marabasco river estuary. However more sedimentary evidence needs to be collected at other sites across this wetland to map the lateral extent of this deposit and corroborate this hypothesis.

5.3. Alternative mechanism for the creation of contact A

The Mexican Pacific coast is frequently affected by large hurricanes, which can produce significant geomorphological changes, increasing rapidly the penetration of marine waters and deposition of littoral sediments in coastal wetlands, producing similar stratigraphic sequences to those created by earthquakes and tsunamis (e.g. Peterson & Darienzo, 1991; Nelson et al., 1998; Otvos, 2011; Goslin & Clemmensen, 2017). Here we test as an alternative hypothesis, the origin of Contact A to be product of hurricane Winifred (1992 CE) or hurricane Calvin (1993 CE). These events were the biggest hurricanes that occurred between 1985 – 2003 CE, which made landfall in a 50 km radius of the study site (**Figure S.1 in supplementary material**), which corresponds to the area from the eye of a hurricane with the highest likelihood to produce significant geomorphological changes and washover deposits in low-lying areas (Morton & Sallenger, 2003).

Hurricane Winifred was an event that formed on October 6, 1992. This event reached a category 3, of the Saffir-Simpson hurricane scale, on October 9, producing wind velocities that peak at 185 km/hr offshore the coast of Michoacan, roughly 183 km southeast of Estero Potrero Grande (NHC, 1992). Some hours later on the same day, Winifred made landfall as a hurricane category 2 in the Manzanillo bay, 30 km south east of the study site (NHC, 1992).

Hurricane Calvin formed offshore the coast of Oaxaca on July 4, 1993. At its peak intensity, hurricane category 2, it reached wind velocities of 175 km/hr (NHC, 1993). Three days after its formation, Calvin made landfall as a hurricane category 2, close to the mouth of the Cuixmala river, which lies approximately 50 km northwest of Estero Potrero Grande. At the moment of landfall, the maximum windspeed registered was 157 km/hr (NHC, 1993).

Instrumental observations of storm surges and water levels produced by these hurricanes are unspecified, as well as the erosive and depositional imprints along the coast. Hence, to test our alternative hypothesis, we compare hurricanes Winifred and Calvin with the characteristics (NOAA, 2004, 2009; NHC, 2021) and impacts (Morton et al., 2007; Conery et al., 2018; FDEP, 2020) of three hurricanes that made landfall as category 2 in the US Gulf of Mexico coast and US Atlantic coast (**Table 1**). These hurricanes produced storm surges at the site of landfall between 1.68 - 2.83 m. Considering that storm surges are caused by strong winds and low atmospheric pressures; comparing these parameters among all hurricanes in table 1, it seems very unlikely that hurricanes Winifred and Calvin could produce storm surges of such magnitudes, not only because they record lower wind speed and higher atmospheric pressure, but also because the ocean waters in the Pacific coast are deeper than the gently slope coasts in the Atlantic and Gulf of Mexico, limiting the height of storm surges (NHC, 1993).

Table 1. Comparison of characteristics of hurricanes Winifred and Calvin with other hurricanes of similar intensities.

Event	Hurricane Winifred	Hurricane Calvin	Hurrican Isabel	Hurricane Ike	Hurricane Sally
Year	1992	1993	2003	2008	2020
Region	Mexican Pacific coast	Mexican Pacific coast	US Atlantic coast	US Gulf of Mexico coast	US Gulf of Mexico coast
Maximum category	3	2	5	4	2
Maximum wind speed (km/hr)	185	175	268	231	95
Minimum pressure (mb)	960	966	915	935	965
Landfall site	Cuixmala river, Jalisco	Manzanillo bay, Colima	Drum Inlet, North Carolina	Galveston Bay, Texas	Gulf Shores, Alabama
Catregory at landfall	2	2	2	2	2
Windspeed at landfall (km/hr)	157	157	167	175	176
Pressure at landfall (mb)	975	973	957	950	965
Maximum storm surge (m)	-----	-----	2.47	2.83	1.68
Maximum water level (m NAVD88)	-----	-----	2.49	3.25	1.99
Maximum water level (m MHHW)	-----	-----	2.17	2.915	1.705
Region affected			Northern Outer banks, North Carolina	Eastern Texas and western Louisiana	Santa Rosa island, northwestern Florida
Local geomorphology	Coastal barrier, 200 - 400 m wide, composed by a series of beach ridges and a chain of frontal dunes (> 5 m), backed by mangrove swamps.		Narrow barrier islands (< 200 m wide) with dunes systems (< 5 m high), backed by marsh lands	Narrow beaches and low chenier plains (1 - 2 m high), backed by marsh lands	Barrier islands with dune systems (<10 m) backed by Pensacola bay.
Impacts			Creation of a washover terrace, ~400 m inland, and coastal breaching.	Floods > 10 km and washover deposits ~100 m.	Intense dune erosion with overwash deposits ~300 m inland.
Source			NOAA, 2004; Conery et al. 2008; Morton et al. 2007	NOAA, 2009; Doran et al. 2009	NHC, 2021; FDEP, 2020

In addition to atmospheric pressure, wind velocities and coastal slope, other local factors could have played an important role in the creation of high storm surges during hurricanes Winifred or

Calvin. Nonetheless, even in a worse-case scenario such as hurricane Ike (**Table 1**), water levels would not be high enough to overtop the barrier due to the local topographic conditions, which play a major control to limit coastal flooding and washover deposition (Soria et al., 2017; Watanabe et al., 2017). This coastal barrier hosts a chain of frontal dunes at least 5 m above mean sea level and a sequence of higher beach rides that extend inland for at least 400 m. (e.g. Méndez Linares et al., 2007; Zuber et al., 2022) Coastal floods caused by hurricane Winifred were only reported at the town of Cuyutlan (Padilla Lozoya, 2007), which is more than 50 km southeast from Estero Potrero Grande. Indeed, most of the damages produced by this event were identified in the southern portion of Colima and Michoacán (NHC, 1992). This region lies on the right-front quadrant of hurricane Winifred, which is the location where the storm surge, onshore-directed winds, and waves focus their greatest energy (Morton & Sallenger, 2003; Doran et al., 2009). For hurricane Calvin, official reports do not indicate floods in the coastal plain of the Marabasco river (e.g. Hernández et al., 2013). Even though the study site was on the right-front quadrant of hurricane Calvin, the obliquity of the hurricane track to this coastal stretch was a factor that reduced the income energy to produce high water levels (**Figure S.1 in supplementary material**).

Satellite images of post-hurricanes show no evidence of wave overtopping nor coastal breaching along the barrier (**Figure S.2 in supplementary material**). The only breached site that could have facilitated the incursion of marine waters in this study site is the Marabasco river mouth. When the mouth of the river breaches it is often due to high-water levels produced by fluvial discharges, occurring before a hurricane hits the coast (e.g. Elwany et al., 1998; McSweeney et al., 2017). If high fluvial discharge interacts with a storm surge and waves, the wetland may experience an increase in brackish and marine waters. Nonetheless, local factors such as the meandering pattern of the creek channels, the distance of the coring sites to the river mouth (2.6 km) and the presence of mangrove patches would have reduced the capacity of the storm surge and waves to reach the coring sites. After more recent and intense hurricanes, we have observed that only creek bank locations that cut the back barrier wetland are able to produce significant sedimentary changes in response to high fluvial discharges rather than storm surge and wave deposits.

Lastly, if any of these hurricanes produced significant morphological changes at the river mouth, such changes could amplify the tidal prism, increasing the influence of marine waters and sediments at the coring sites. However, it is unlikely that a hurricane of category 2 would cause a long-lasting change in the sedimentary regime of the wetland because in this wave-dominated settings breaching events are short-lived due to the lack of sustained inlet flow after the driven event (e.g. Rich & Keller, 2013; Seminack & McBride, 2018). Our diatomological and geochemical data show a long-lasting change from a freshwater to a brackish-marine environment, which cannot be explained by a short-lived marine incursion caused by a minor hurricane. Consequently, our observations and reconstructions lead us to conclude that contact A is unlikely to be the signature of hurricane Winifred nor hurricane Calvin.

5.4. Implications for further paleoseismic investigations.

Our findings demonstrate that fossil diatoms are well preserved in fine-grained sedimentary sequences of back-barrier coastal wetlands along the Mexican Pacific. Previous studies of megathrust earthquakes along the Mexican Subduction Zone have noticed the low concentrations and poor preservation of microfossils in coastal deposits, particularly in sandy rich settings and mangrove environments (e.g. Ramírez-Herrera et al., 2012, 2014, 2016). Here, we demonstrate that the high abundance of fossil diatoms in back-barrier settings opens the possibility to use them in future investigations as a geological proxy to quantify relative sea-level changes produced coseismically, complementing tsunami investigations along the Mexican subduction zone.

This approach has the potential to investigate earlier earthquakes allowing reconstruction of multiple earthquake deformation cycles through the pre-instrumental earthquakes improving our understanding of the, unclear, pattern of longer-term coastal deformation (e.g. Ramírez-Herrera et al., 2004). Understanding variable coseismic land-level changes across multiple earthquake deformation cycles offers a unique opportunity to understand down-dip rupture variations (e.g. Nelson et al., 2008; Briggs et al., 2014; Dura et al., 2017). This would provide an opportunity to refine the earthquake hazard assessment of this region, as deeper ruptures represent a major hazard to coastal and inland territories due to their proximity to the seismic source.

6. Conclusions.

The 1995 Colima-Jalisco earthquake produced coastal subsidence, recorded in the stratigraphy of the wetland Estero Potrero Grande. The lithological expression of this sudden RSL rise is a horizontal bed of organic silt overlain abruptly by a bed of grey silt, which extends laterally for over 1 km, with an age of 1995 CE. We demonstrate that the overlying silt unit is accompanied by a rapid increase in salinity conditions, shown by the elemental log-ratios and diatom assemblages. Two diatom-based paleoelevation reconstructions suggest subsidence in the order of 0.06 ± 0.05 m and 0.11 ± 0.16 m. These reconstructions are consistent with the magnitude of subsidence recorded by GPS observations and tide gauge data along the coast adjacent to the earthquake rupture. The stratigraphy also shows evidence of a brief period of RSL fall, reflecting post-seismic uplift, followed by a period of gradual RSL rise, interpreted as the beginning of the interseismic stage. A millimetric laminae of sand accompanying the submergence of the wetland reveals the minimal signature of the event of the tsunami that accompanied this earthquake.

In this study we develop the first diatom-based study designed to quantify the magnitude of coastal coseismic subsidence on the Mexican Pacific coast. The approach we develop demonstrates the feasibility of fossil diatoms to quantify decimeter-scale relative sea-level changes, even with the lack of a local modern dataset of diatom assemblages. Nonetheless, to better constrain relative sea-level reconstructions and reduce their uncertainties, we encourage future investigations along this coast to build transfer function models based on modern assemblages from the Mexican Pacific coast. Our findings can complement existing evidence of past earthquakes focusing on tsunami deposits and if applied to deeper sediment sequences should allow for a more complete understanding of the unknown behavior of the Mexican subduction zone.

Acknowledgments

This research was carried out during the Doctoral studies of EBF. This project was supported by the scholarship for Mexican Doctoral Students awarded by Consejo Nacional de Ciencia y Tecnologia (CONACyT). Financial support to carry out fieldwork was provided by the Latin America Mobility Grant of Santander Universities, New Research Workers' Award of the Quaternary Research Association, Postgraduate Research Grant of the Department of Geography of Durham University, MCR Research award of Hatfield College of Durham University and the Charles Boyden Fund for Small Grants of the Estuarine and Coastal Sciences Association. Funding for radiocarbon dating was obtained through the NERC Grant-in-kind. We acknowledge Ana Patricia Mendez Linares, Jose Ramon Hernandez Santana, Andrea Mancera, Emilio Saavedra and Adrián Ciprés for supporting fieldwork. Lastly, we thank Ed Garrett for providing us with the diatom dataset from Chile. This paper is a contribution to IGCP 725 project “Forecasting coastal change.”

Data availability

Raw data is provided in the excel file named “Supplementary_Material_Tables”.

References

Abbott, E. R., & Brudzinski, M. R. (2015). Shallow seismicity patterns in the northwestern section of the Mexico Subduction Zone. *Journal of South American Earth Sciences*, *63*, 279–292. https://doi.org/10.1016/j.jsames.2015.07.012

Abràmoff, M. D., Magalhaes, P. J., & Sunanda, J. R. (2004). Image Processing with ImageJ. *Biophotonics International*, *11*(7), 7.

Atwater, B. F. (1987). Evidence for Great Holocene Earthquakes Along the Outer Coast of Washington State. *Science*, *236*, 942–944. https://doi.org/10.1126/science.236.4804.942

Atwater, B. F. (1992). Geologic evidence for earthquakes during the past 2000 years along the Copalis River, southern coastal Washington. *Journal of Geophysical Research: Solid Earth*, *97*(B2), 1901–1919. https://doi.org/10.1029/91JB02346

Atwater, B. F., Nelson, A. R., Clague, J. J., Carver, G. A., Yamaguchi, D. K., Bobrowsky, P. T., Bourgeois, J., Darienzo, M. E., Grant, W. C., Hemphill-Haley, E., Kelsey, H. M., Jacoby, G. C., Nishenko, S. P., Palmer, S. P., Peterson, C. D., & Reinhart, M. A. (1995). Summary of Coastal Geologic Evidence for Past Great Earthquakes at the Cascadia Subduction Zone. *Earthquake Spectra*, *11*(1), 1–18. https://doi.org/10.1193/1.1585800

Azúa, B. M., DeMets, C., & Masterlark, T. (2002). Strong interseismic coupling, fault afterslip, and viscoelastic flow before and after the Oct. 9, 1995 Colima-Jalisco earthquake: Continuous GPS measurements from Colima, Mexico. *Geophysical Research Letters*, *29*(8), 1-4. https://doi.org/10.1029/2002GL014702

Bandy, W., Kostoglodov, V., Díaz, A. H., & Mena, M. (1999). Structure of the southern Jalisco subduction zone, Mexico, as inferred from gravity and seismicity. *Geofísica Internacional*, *38*(3), 127–136.

Barlow, N. L. M., Shennan, I., Long, A. J., Gehrels, W. R., Saher, M. H., Woodroffe, S. A., & Hillier, C. (2013). Salt marshes as late Holocene tide gauges. *Global and Planetary Change*, *106*, 90–110. https://doi.org/10.1016/j.gloplacha.2013.03.003

Bate, N., & Newall, P. (2002). Techniques for the use of diatoms in water quality assessment: How many valves? *Proceedings of the 15th International Diatom Symposium*.

Bianchette, T. A., Liu, K., & McCloskey, T. A. (2022). A 4000-year paleoenvironmental reconstruction and extreme event record from Laguna Nuxco, Guerrero, Mexico.

Palaeogeography, Palaeoclimatology, Palaeoecology, *594*, 1-13. https://doi.org/10.1016/j.palaeo.2022.110933

Bianchette, T. A., McCloskey, T. A., & Liu, K. (2016). Re-Evaluating the Geological Evidence for Late Holocene Marine Incursion Events along the Guerrero Seismic Gap on the Pacific Coast of Mexico. *PLOS ONE*, *11*(8), 1-14. https://doi.org/10.1371/journal.pone.0161568

Bianchette, T. A., McCloskey, T. A., & Liu, K. (2017). A 7000-year history of coastal environmental changes from Mexico's Pacific coast: A multi-proxy record from Laguna Mitla, Guerrero. *The Holocene*, *27*(8), 1214–1226. https://doi.org/10.1177/0959683616687379

Birks, H. J. B. (2005). Quantitative palaeoenvironmental reconstructions from Holocene biological data. In H. J. B. Birks, R. Battarbee, A. Mackay, & F. Oldfield (Eds.), *Global Change in the Holocene* (p. 17).

Blott, S. J., & Pye, K. (2001). GRADISTAT: A grain size distribution and statistics package for the analysis of unconsolidated sediments. *Earth Surface Processes and Landforms*, *26*(11), 1237–1248. https://doi.org/10.1002/esp.261

Bodin, P., & Klinger, T. (1986). Coastal Uplift and Mortality of Intertidal Organisms Caused by the September 1985 Mexico Earthquakes. *Science*, *233*(4768), 1071–1073.

Bógalo, M. F., Ramírez-Herrera, M.-T., Goguitchaichvili, A., Rey, D., Mohamed, K. J., Calvo-Rathert, M., & Corona, N. (2017). Magnetic signature of the 22 June 1932 tsunami deposits (Jalisco, Mexican Pacific coast): Magnetic signature of tsunami deposits. *Geochemistry, Geophysics, Geosystems*, *18*(6), 2370–2387. https://doi.org/10.1002/2016GC006752

Borerro, J., Ortiz, M., Titov, V., & Synolakis, C. (1997). Field survey of Mexican tsunami produces new data, unusual photos. *Eos, Transactions American Geophysical Union*, *78*(8), 85–88. https://doi.org/10.1029/97EO00054

Brader, M., Garrett, E., Melnick, D., & Shennan, I. (2021). Sensitivity of tidal marshes as recorders of major megathrust earthquakes: Constraints from the 25 December 2016 M_w 7.6 Chiloé earthquake, Chile. *Journal of Quaternary Science*, *36*(6), 991–1002. https://doi.org/10.1002/jqs.3323

Briggs, R. W., Engelhart Simon E., Nelson Alan R., Dura Tina, Kemp Andrew C., Haeussler Peter J., Corbett D. Reide, Angster Stephen J., & Bradley Lee-Ann. (2014). Uplift and subsidence reveal a nonpersistent megathrust rupture boundary (Sitkinak Island, Alaska).

Geophysical Research Letters, *41*(7), 2289–2296. https://doi.org/10.1002/2014GL059380

Buenfil-López, L. A., Rebollar-Plata, M., Muñoz-Sevilla, N. P., & Juárez-León, B. (2012). Sea-Level Rise and Subsidence/Uplift Processes in the Mexican South Pacific Coast. *Journal of Coastal Research*, *28*(5), 1154–1164. https://doi.org/10.2112/JCOASTRES-D-11-00118.1

Castillo-Aja, R., Ramírez-Herrera, M.-T., Machain-Castillo, M. L., Goguitchaichvili, A., & Cejudo, R. (2019). Sedimentary and microfossil imprint from historical earthquakes and tsunamis, Jalisco coast, Mexican subduction. *Marine Geology*, *407*, 32–43. https://doi.org/10.1016/j.margeo.2018.10.004

Černý, J., Ramirez-Herrera, M. T., Bógalo, M. F., Goguitchaichvili, A., Castillo-Aja, R., Morales, J., Sanchez-Cabeza, J. A., & Ruiz-Fernández, A. C. (2015). Magnetic record of extreme marine inundation events at Las Salinas site, Jalisco, Mexican Pacific coast. *International Geology Review*, *58*(3), 342-357, https://doi.org/10.1080/00206814.2015.1075230.

Chagué, C., Sugawara, D., Goto, K., Goff, J., Dudley, W., & Gadd, P. (2018). Geological evidence and sediment transport modelling for the 1946 and 1960 tsunamis in Shinmachi, Hilo, Hawaii. *Sedimentary Geology*, *364*, 319–333. https://doi.org/10.1016/j.sedgeo.2017.09.010

Chagué-Goff, C., Goff, J., Wong, H. K. Y., & Cisternas, M. (2015). Insights from geochemistry and diatoms to characterise a tsunami's deposit and maximum inundation limit. *Marine Geology*, *359*, 22–34. https://doi.org/10.1016/j.margeo.2014.11.009

Chagué-Goff, C., Szczuciński, W., & Shinozaki, T. (2017). Applications of geochemistry in tsunami research: A review. *Earth-Science Reviews*, *165*, 203–244. https://doi.org/10.1016/j.earscirev.2016.12.003

Cisternas, M., Atwater, B. F., Torrejón, F., Sawai, Y., Machuca, G., Lagos, M., Eipert, A., Youlton, C., Salgado, I., Kamataki, T., Shishikura, M., Rajendran, C. P., Malik, J. K., Rizal, Y., & Husni, M. (2005). Predecessors of the giant 1960 Chile earthquake. *Nature*, *437*(7057), 404–407. https://doi.org/10.1038/nature03943

Cocquyt, C., Ndjombo, E. L., Tsamemba, S. T., & Malale, H. N. S. wa. (2019). Freshwater diatoms in the Democratic Republic of the Congo: A historical overview of the research and publications. *PhytoKeys*, *136*, 107–125. https://doi.org/10.3897/phytokeys.136.47386

Compère, P. (1984). Some algae from the Red Sea Hills in north-eastern Sudan. In H. J. Dumont, A. I. el Moghraby, & L. A. Desougi (Eds.), *Limnology and Marine Biology in the Sudan* (pp. 61–77). Springer Netherlands. https://doi.org/10.1007/978-94-009-6557-7_8

Conery, I., Walsh, J. P., & Corbett, D. R. (2018). Hurricane Overwash and Decadal-Scale Evolution of a Narrowing Barrier Island, Ocracoke Island, NC. *Estuaries and Coasts*, *41*(6), 1626–1642. https://doi.org/10.1007/s12237-018-0374-y

Corbett, D. R., & Walsh, J. P. (2015). 210-Lead and 137-Cesium: Establishing a chronology for the last century. In I. Shennan, A. J. Long, & B. P. Horton (Eds.), *Handbook of Sea-Level Research* (pp. 361–372). John Wiley & Sons, Ltd. https://doi.org/10.1002/9781118452547.ch24

Cordero-Oviedo, C., Correa-Metrio, A., Urrego, L. E., Vázquez, G., Blaauw, M., Escobar, J., & Curtis, J. H. (2019). Holocene establishment of mangrove forests in the western coast of the Gulf of Mexico. *CATENA*, *180*, 212–223. https://doi.org/10.1016/j.catena.2019.04.025

Corona, N., & Ramírez-Herrera, M. T. (2012). Mapping and historical reconstruction of the great Mexican 22 June 1932 tsunami. *Natural Hazards and Earth System Sciences*, *12*(5), 1337–1352. https://doi.org/10.5194/nhess-12-1337-2012

Corona, N., & Ramírez-Herrera, M.-T. (2015). Did an underwater landslide trigger the June 22, 1932 tsunami off the Pacific coast of Mexico? *Pure and Applied Geophysics*, *172*(12), 3573–3587. https://doi.org/10.1007/s00024-015-1171-1

Cosenza-Muralles, B., DeMets, C., Márquez-Azúa, B., Sánchez, O., Stock, J., Cabral-Cano, E., & McCaffrey, R. (2021a). Co-seismic and post-seismic deformation for the 1995 Colima–Jalisco and 2003 Tecomán thrust earthquakes, Mexico subduction zone, from modelling of GPS data. *Geophysical Journal International*, *228*(3), 2137–2173. https://doi.org/10.1093/gji/ggab435

Cosenza-Muralles, B., DeMets, C., Márquez-Azúa, B., Sánchez, O., Stock, J., Cabral-Cano, E., & McCaffrey, R. (2021b). GPS-derived interseismic fault locking along the Jalisco–Colima segment of the Mexico subduction zone. *Geophysical Journal International*, *228*(3), 2174–2197. https://doi.org/10.1093/gji/ggab436

Courboulex, F., Singh, S. K., Pacheco, J. F., & Ammon, C. J. (1997). The 1995 Colima-Jalisco, Mexico, Earthquake (Mw 8): A study of the rupture process. *Geophysical Research Letters*, *24*(9), 1019–1022. https://doi.org/10.1029/97GL00945

Dañobeitia, J., Bartolomé, R., Prada, M., Nuñez-Cornú, F., Córdoba, D., Bandy, W. L., Estrada, F., Cameselle, A. L., Nuñez, D., Castellón, A., Alonso, J. L., Mortera, C., & Ortiz, M. (2016). Crustal Architecture at the Collision Zone Between Rivera and North American Plates at the Jalisco Block: Tsujal Project. *Pure and Applied Geophysics*, *173*(10–11), 3553–3573. https://doi.org/10.1007/s00024-016-1388-7

De la Lanza Espino, G. J., Ortiz Pérez, M. A., & Carbajal Pérez, J. L. (2013). Diferenciación hidrogeomorfológica de los ambientes costeros del Pacífico, del Golfo de México y del Mar Caribe. *Investigaciones Geográficas*, *81*. https://doi.org/10.14350/rig.33375

DeMets, C., Carmichael, I., Melbourne, T., Sanchez, O., Stock, J., Suarez, G., & Hudnut, K. (1995). Anticipating the successor to Mexico's largest historical earthquake. *Eos, Transactions American Geophysical Union*, *76*(42), 413–413. https://doi.org/10.1029/95EO00255

Denys, L. (1991). A check-list of the diatoms in the Holocene deposits of the Western Belgian coastal plain with the survey of their apparent ecological requirements. Introduction, ecological code and complete list. (Vol. 246). Geological Service of Belgium.

DePaolis, J. M., Dura, T., MacInnes, B., Ely, L. L., Cisternas, M., Carvajal, M., Tang, H., Fritz, H. M., Mizobe, C., Wesson, R. L., Figueroa, G., Brennan, N., Horton, B. P., Pilarczyk, J. E., Corbett, D. R., Gill, B. C., & Weiss, R. (2021). Stratigraphic evidence of two historical tsunamis on the semi-arid coast of north-central Chile. *Quaternary Science Reviews*, *266*, 107052. https://doi.org/10.1016/j.quascirev.2021.107052

Dominguez Rivas, J., Singh, S. K., & Sánchez Sesma, F. (1997). Sismología. In A. Tena-Colunga (Ed.), *El macrosismo de Manzanillo del 9 de octubre de 1995: Colima, México, septiembre de 1997*. Universidad de Colima : Gobierno del Estado de Colima : Sociedad Mexicana de Ingeniería Sísmica.

Doran, K. S., Plant, N. G., Stockdon, H. F., Sallenger, A. H., & Serafin, K. A. (2009). *Hurricane Ike: Observations and Analysis of Coastal Change* (p. 35) [USGS Open-File Report 2009-1061]. USGS. https://pubs.usgs.gov/of/2009/1061/

Drexler, J. Z., Fuller, C. C., & Archfield, S. (2018). The approaching obsolescence of 137Cs dating of wetland soils in North America. *Quaternary Science Reviews*, *199*, 83–96. https://doi.org/10.1016/j.quascirev.2018.08.028

Dura, T., Hemphill-Haley, E., Sawai, Y., & Horton, B. P. (2016). The application of diatoms to reconstruct the history of subduction zone earthquakes and tsunamis. *Earth-Science Reviews*, *152*, 181–197. https://doi.org/10.1016/j.earscirev.2015.11.017

Dura, T., Horton, B. P., Cisternas, M., Ely, L. L., Hong, I., Nelson, A. R., Wesson, R. L., Pilarczyk, J. E., Parnell, A. C., & Nikitina, D. (2017). Subduction zone slip variability during the last millennium, south-central Chile. *Quaternary Science Reviews*, *175*, 112–137. https://doi.org/10.1016/j.quascirev.2017.08.023

Dura, T., Rubin, C. M., Kelsey, H. M., Horton, B. P., Hawkes, A., Vane, C. H., Daryono, M., Pre, C. G., Ladinsky, T., & Bradley, S. (2011). Stratigraphic record of Holocene coseismic subsidence, Padang, West Sumatra. *Journal of Geophysical Research: Solid Earth*, *116*(B11), B11306. https://doi.org/10.1029/2011JB008205

Elwany, M. H. S., Flick, R. E., & Aijaz, S. (1998). Opening and closure of a marginal Southern California lagoon inlet. *Estuaries*, *21*(2), 246–254. https://doi.org/10.2307/1352472

Escobedo, D., Pacheco, J. F., & Suárez, G. (1998). Teleseismic body-wave analysis of the 9 October, 1995 (Mw = 8.0), Colima-Jalisco, Mexico Earthquake, and its largest foreshock and aftershock. *Geophysical Research Letters*, *25*(4), 547–550. https://doi.org/10.1029/98GL00061

Farreras, S., Ortiz, M., & Gonzalez, J. I. (2007). Steps Towards the Implementation of a Tsunami Detection, Warning, Mitigation and Preparedness Program for Southwestern Coastal Areas of Mexico. *Pure and Applied Geophysics*, *164*(2–3), 605–616. https://doi.org/10.1007/s00024-006-0175-2

FDEP (2020). *Hurricane Sally Post-Storm Beach Conditions and Coastal Impact Report* (p. 57).

Figueroa-Rangel, B. L., Valle-Martínez, A., Olvera-Vargas, M., & Liu, K. (2016). Environmental History of Mangrove Vegetation in Pacific West-Central Mexico during the Last 1300 Years. *Frontiers in Ecology and Evolution*, *4*. https://doi.org/10.3389/fevo.2016.00101

Folk, R. L., & Ward, W. C. (1957). *Brazos River Bar: A Study in the Significance of Grain Size Parameters*. 24.

Fujiwara, O., Goto, K., Ando, R., & Garrett, E. (2020). Paleotsunami research along the Nankai Trough and Ryukyu Trench subduction zones – Current achievements and future challenges. *Earth-Science Reviews*, *210*, 103333. https://doi.org/10.1016/j.earscirev.2020.103333

Garrett, E., Fujiwara, O., Garrett, P., Heyvaert, V. M. A., Shishikura, M., Yokoyama, Y., Hubert-Ferrari, A., Brückner, H., Nakamura, A., & De Batist, M. (2016). A systematic review of geological evidence for Holocene earthquakes and tsunamis along the Nankai-Suruga

Trough, Japan. *Earth-Science Reviews*, *159*, 337–357. https://doi.org/10.1016/j.earscirev.2016.06.011

Garrett, E., Shennan, I., Watcham, E. P., & Woodroffe, S. A. (2013). Reconstructing paleoseismic deformation, 1: Modern analogues from the 1960 and 2010 Chilean great earthquakes. *Quaternary Science Reviews*, *75*, 11–21. https://doi.org/10.1016/j.quascirev.2013.04.007

Garrett, E., Shennan, I., Woodroffe, S. A., Cisternas, M., Hocking, E. P., & Gulliver, P. (2015). Reconstructing paleoseismic deformation, 2: 1000 years of great earthquakes at Chucalén, south central Chile. *Quaternary Science Reviews*, *113*, 112–122. https://doi.org/10.1016/j.quascirev.2014.10.010

Goslin, J., & Clemmensen, L. B. (2017). Proxy records of Holocene storm events in coastal barrier systems: Storm-wave induced markers. *Quaternary Science Reviews*, *174*, 80–119. https://doi.org/10.1016/j.quascirev.2017.08.026

Gouramanis, C., Switzer, A. D., Jankaew, K., Bristow, C. S., Pham, D. T., & Ildefonso, S. R. (2017). High-frequency Coastal Overwash Deposits from Phra Thong Island, Thailand. *Scientific Reports*, *7*(1). https://doi.org/10.1038/srep43742

Govers, R., Furlong, P., Wiel, L., Herman, W., & Broerse, T. (2017). The Geodetic Signature of the Earthquake Cycle at Subduction Zones: Model Constraints on the Deep Processes. *Reviews of Geophysics*, *56, 6-49*. https://doi.org/10.1002/2017RG000586

Hamilton, S., & Shennan, I. (2005). Late Holocene relative sea-level changes and the earthquake deformation cycle around upper Cook Inlet, Alaska. *Quaternary Science Reviews*, *24*(12), 1479–1498. https://doi.org/10.1016/j.quascirev.2004.11.003

Hamilton, S., Shennan, I., Combellick, R., Mulholland, J., & Noble, C. (2005). Evidence for two great earthquakes at Anchorage, Alaska and implications for multiple great earthquakes through the Holocene. *Quaternary Science Reviews*, *24*(18), 2050–2068. https://doi.org/10.1016/j.quascirev.2004.07.027

Hartley, B., Barber, H. G., Carter, J. R., & Sims, P. A. (1996). *An atlas of British diatoms*. Biopress. 601 p.

Haslett, J., & Parnell, A. (2008). A simple monotone process with application to radiocarbon-dated depth chronologies. *Journal of the Royal Statistical Society: Series C (Applied Statistics)*, *57*(4), 399–418. https://doi.org/10.1111/j.1467-9876.2008.00623.x

Hemphill-Haley, E. (1996). Diatoms as an aid in identifying late-Holocene tsunami deposits. *The Holocene*, *6*(4), 439–448. https://doi.org/10.1177/095968369600600406

Hernández, J. C. M., Molina, L. M. F., González, F. M.-C., López, V. M. C., & López, J. T. (2013). Influencia de los ciclones tropicales del periodo de 1970 al 2010 en la región de Bahía de Banderas, Nayarit-Jalisco, México*, México*. 21(59), 13-24.

Hernández Santana, J. R., Ortiz Pérez, M. A., & Zamorano Orozco, J. J. (1995). Regionalización morfoestructural de la Sierra Madre del Sur, México. *Investigaciones geográficas*, *31*, 45–67.

Hill, T. D., Sommer, N. R., Kanaskie, C. R., Santos, E. A., & Oczkowski, A. J. (2018). Nitrogen uptake and allocation estimates for Spartina alterniflora and Distichlis spicata. *Journal of Experimental Marine Biology and Ecology*, *507*, 53–60. https://doi.org/10.1016/j.jembe.2018.07.006

Hjörleifsdóttir, V., Sánchez-Reyes, H. S., Ruiz-Angulo, A., Ramírez-Herrera, M. T., Castillo-Aja, R., Singh, S. K., & Ji, C. (2018). Was the 9 October 1995 Mw 8 Jalisco, Mexico, Earthquake a Near-Trench Event? *Journal of Geophysical Research: Solid Earth*, *123*(10), 8907–8925. https://doi.org/10.1029/2017JB014899

Hocking, E. P., Garrett, E., & Cisternas, M. (2017). Modern diatom assemblages from Chilean tidal marshes and their application for quantifying deformation during past great earthquakes. *Journal of Quaternary Science*, *32*(3), 396–415. https://doi.org/10.1002/jqs.2933

Horton, B. P., & Sawai, Y. (2010). Diatoms as indicators of former sea levels, earthquakes, tsunamis, and hurricanes. In J. P. Smol & E. F. Stoermer (Eds.), *The Diatoms* (2nd ed., pp. 357–372). Cambridge University Press. https://doi.org/10.1017/CBO9780511763175.020

Horton, B. P., Zong, Y., Hillier, C., & Engelhart, S. (2007). Diatoms from Indonesian mangroves and their suitability as sea-level indicators for tropical environments. *Marine Micropaleontology*, *63*(3), 155–168. https://doi.org/10.1016/j.marmicro.2006.11.005

Hua, Q., Turnbull, J. C., Santos, G. M., Rakowski, A. Z., Ancapichún, S., Pol-Holz, R. D., Hammer, S., Lehman, S. J., Levin, I., Miller, J. B., Palmer, J. G., & Turney, C. S. M. (2021). Atmospheric Radiocarbon For The Period 1950–2019. *Radiocarbon*, 1–23. https://doi.org/10.1017/RDC.2021.95

Hutton, W., DeMets, C., Sánchez, O., Suárez, G., & Stock, J. (2001). Slip kinematics and dynamics during and after the 1995 October 9 Mw = 8.0 Colima–Jalisco earthquake, Mexico, from GPS geodetic constraints. *Geophysical Journal International*, *146*(3), 637–658. https://doi.org/10.1046/j.1365-246X.2001.00472.x

INEGI. (1975). *Carta uso del suelo, Cihuatlán E-13-B-42* [Map].

Jankaew, K., Atwater, B. F., Sawai, Y., Choowong, M., Charoentitirat, T., Martin, M. E., & Prendergast, A. (2008). Medieval forewarning of the 2004 Indian Ocean tsunami in Thailand. *Nature*, *455*(7217), Article 7217. https://doi.org/10.1038/nature07373

Jaramillo, D., Vélez, M. I., Escobar, J., Pardo-Trujillo, A., Vallejo, F., Villegas, J. C., Acevedo, A. L., Curtis, J., Rincón, H., & Trejos-Tamayo, R. (2021). Mid to late holocene dry events in Colombia's super humid Western Cordillera reveal changes in regional atmospheric circulation. *Quaternary Science Reviews*, *261*, 106937. https://doi.org/10.1016/j.quascirev.2021.106937

Kelsey, H. M., Nelson, A. R., Hemphill-Haley, E., & Witter, R. C. (2005). Tsunami history of an Oregon coastal lake reveals a 4600 yr record of great earthquakes on the Cascadia subduction zone. *GSA Bulletin*, *117*(7–8), 1009–1032. https://doi.org/10.1130/B25452.1

Kelsey, H. M., Witter, R. C., Engelhart, S. E., Briggs, R., Nelson, A., Haeussler, P., & Corbett, D. R. (2015). Beach ridges as paleoseismic indicators of abrupt coastal subsidence during subduction zone earthquakes, and implications for Alaska-Aleutian subduction zone paleoseismology, southeast coast of the Kenai Peninsula, Alaska. *Quaternary Science Reviews*, *113*, 147–158. https://doi.org/10.1016/j.quascirev.2015.01.006

Kemp, A. C., Cahill, N., Engelhart, S. E., Hawkes, A. D., & Wang, K. (2018). Revising Estimates of Spatially Variable Subsidence during the A.D. 1700 Cascadia Earthquake Using a Bayesian Foraminiferal Transfer Function. *Bulletin of the Seismological Society of America*, *108*(2), 654–673. https://doi.org/10.1785/0120170269

Kemp, A. C., & Telford, R. J. (2015). Transfer functions. In I. Shennan, A. J. Long, & B. P. Horton (Eds.), *Handbook of Sea-Level Research* (pp. 470–499). John Wiley & Sons, Ltd. https://doi.org/10.1002/9781118452547.ch31

Kempf, P., Moernaut, J., Van Daele, M., Pino, M., Urrutia, R., & De Batist, M. (2020). Paleotsunami record of the past 4300 years in the complex coastal lake system of Lake Cucao, Chiloé Island, south central Chile. *Sedimentary Geology*, *401*, 105644. https://doi.org/10.1016/j.sedgeo.2020.105644

Kostoglodov, V., & Pacheco, J. (1999). *Cien anos de sismicidad en México*. Universidad Nacional Autónoma de México. http://usuarios.geofisica.unam.mx/vladimir/sismos/100a%F1os.html

Lankford, R. R. (1977). Coastal lagoons of Mexico their origin and classication. In *Estuarine Processes* (pp. 182–215). Elsevier. https://doi.org/10.1016/B978-0-12-751802-2.50022-9

León, T., Lau, A. Y. A., Easton, G., & Goff, J. (2023). A comprehensive review of tsunami and palaeotsunami research in Chile. *Earth-Science Reviews*, *236*, 104273. https://doi.org/10.1016/j.earscirev.2022.104273

Lezilda Carvalho Torgan, & Cristiane Bahi Dos Santos. (2008). *Diadesmis confervacea (Diadesmiaceae-Bacillariophyta): Morfologia externa, distribuição e aspectos ecológicos*. https://doi.org/10.13140/2.1.1702.7208

Lonard, R. I., Judd, F. W., & Stalter, R. (2011). The Biological Flora of Coastal Dunes and Wetlands: Batis maritima C. Linnaeus. *Journal of Coastal Research*, *27*(3), 441. https://doi.org/10.2112/JCOASTRES-D-10-00142.1

Long, A. J., & Shennan, I. (1994). Sea-Level Changes in Washington and Oregon and the "Earthquake Deformation Cycle." *Journal of Coastal Research*, *10*(4), 825–838.

López Fuerte, F. O., Siqueiros Beltrones, D. A., & Navaro R. Julio Nelson. (2010). *Benthic diatoms associated with mangrove environments in the northwest region of México*. Editorial de CICIMAR.

López-Fuerte, F. O., & Siqueiros Beltrones, D. A. (2016). A checklist of marine benthic diatoms (Bacillariophyta) from Mexico. *Phytotaxa*, *283*(3), 201. https://doi.org/10.11646/phytotaxa.283.3.1

López-Fuerte, F. O., Siqueiros-Beltrones, D. A., & Hernández-Almeida, O. U. (2013). Epiphytic diatoms of Thalassia testudinum (Hydrocharitaceae) from the Mexican Caribbean. *Marine Biodiversity Records*, *6*, e107. https://doi.org/10.1017/S1755267213000857

Manea, V. C., Manea, M., & Ferrari, L. (2013). A geodynamical perspective on the subduction of Cocos and Rivera plates beneath Mexico and Central America. *Tectonophysics*, *609*, 56–81. https://doi.org/10.1016/j.tecto.2012.12.039

Marmolejo-Rodríguez, A. J., Prego, R., Meyer-Willerer, A., Shumilin, E., & Cobelo-García, A. (2007). Total and labile metals in surface sediments of the tropical river-estuary system of Marabasco (Pacific coast of Mexico): Influence of an iron mine. *Marine Pollution Bulletin*, *55*(10–12), 459–468. https://doi.org/10.1016/j.marpolbul.2007.09.008

Martinez, T., Tejeda, S., Lartigue, J., Zarazua, G., Avila-Perez, P., Ramos, A., Navarrete, M., & Mulller, G. (2014). Chemical composition of marine sediments in the Pacific Ocean from Sinaloa to Jalisco, Mexico. *Journal of Radioanalytical and Nuclear Chemistry*, *299*(1), 827–834. https://doi.org/10.1007/s10967-013-2704-7

Martínez-López, A. (2004). Transport of benthic diatoms across the continental shelf off southern Baja California Peninsula. *Ciencias Marinas*, *30*(4), 503–513. https://doi.org/10.7773/cm.v30i4.347

McQuoid, M. R., & Hobson, L. A. (1998). Assessment of Palaeoenvironmental Conditions on Southern Vancouver Island, British Columbia, Canada, Using the Marine Tychoplankter Paralia Sulcata. *Diatom Research*, *13*(2), 311–321. https://doi.org/10.1080/0269249X.1998.9705453

McQuoid, M. R., & Nordberg, K. (2003). The diatom Paralia sulcata as an environmental indicator species in coastal sediments. *Estuarine, Coastal and Shelf Science*, *56*(2), 339–354. https://doi.org/10.1016/S0272-7714(02)00187-7

McSweeney, S. L., Kennedy, D. M., Rutherfurd, I. D., & Stout, J. C. (2017). Intermittently Closed/Open Lakes and Lagoons: Their global distribution and boundary conditions. *Geomorphology*, *292*, 142–152. https://doi.org/10.1016/j.geomorph.2017.04.022

Melbourne, T., Carmichael, I., DeMets, C., Hudnut, K., Sanchez, O., Stock, J., Suarez, G., & Webb, F. (1997). The geodetic signature of the M8.0 Oct. 9,1995, Jalisco Subduction Earthquake. *Geophysical Research Letters*, *24*(6), 715–718. https://doi.org/10.1029/97GL00370

Meltzner, A. J., Sieh, K., Abrams, M., Agnew, D. C., Hudnut, K. W., Avouac, J.-P., & Natawidjaja, D. H. (2006). Uplift and subsidence associated with the great Aceh-Andaman earthquake of 2004: THE 2004 EARTHQUAKE. *Journal of Geophysical Research: Solid Earth*, *111*. https://doi.org/10.1029/2005JB003891

Méndez Linares, A. P., López-Portillo, J., Hernández-Santana, J. R., Ortiz Pérez, M. A., & Oropeza Orozco, O. (2007). The mangrove communities in the Arroyo Seco deltaic fan, Jalisco, Mexico, and their relation with the geomorphic and physical–geographic zonation. *CATENA*, *70*(2), 127–142. https://doi.org/10.1016/j.catena.2006.05.010

Mendoza, C., & Hartzell, S. (1995). *Fault-Slip Distribution of the 1995 Colima-Jalisco, Mexico, Earthquake*. Bulletin of the Seismological Society of America, 89(5), 1338-1344.

Milker, Y., Nelson, A. R., Horton, B. P., Engelhart, S. E., Bradley, L.-A., & Witter, R. C. (2016). Differences in coastal subsidence in southern Oregon (USA) during at least six prehistoric megathrust earthquakes. *Quaternary Science Reviews*, *142*, 143–163. https://doi.org/10.1016/j.quascirev.2016.04.017

Monecke, K., Finger, W., Klarer, D., Kongko, W., McAdoo, B. G., Moore, A. L., & Sudrajat, S. U. (2008). A 1,000-year sediment record of tsunami recurrence in northern Sumatra. *Nature*, *455*(7217), 1232–1234. https://doi.org/10.1038/nature07374

Monecke, K., Templeton, C. K., Finger, W., Houston, B., Luthi, S., McAdoo, B. G., Meilianda, E., Storms, J. E. A., Walstra, D.-J., Amna, R., Hood, N., Karmanocky, F. J., Nurjanah, Rusydy, I., & Sudrajat, S. U. (2015). Beach ridge patterns in West Aceh, Indonesia, and their response to large earthquakes along the northern Sunda trench. *Quaternary Science Reviews*, *113*, 159–170. https://doi.org/10.1016/j.quascirev.2014.10.014

Moore, A., Nishimura, Y., Gelfenbaum, G., Kamataki, T., & Triyono, R. (2006). Sedimentary deposits of the 26 December 2004 tsunami on the northwest coast of Aceh, Indonesia. *Earth, Planets and Space*, *58*(2), 253–258. https://doi.org/10.1186/BF03353385

Morton, R. A., Gelfenbaum, G., Buckley, M. L., & Richmond, B. M. (2011). Geological effects and implications of the 2010 tsunami along the central coast of Chile. *Sedimentary Geology*, *242*(1), 34–51. https://doi.org/10.1016/j.sedgeo.2011.09.004

Morton, R. A., Gelfenbaum, G., & Jaffe, B. E. (2007). Physical criteria for distinguishing sandy tsunami and storm deposits using modern examples. *Sedimentary Geology*, *200*(3–4), 184–207. https://doi.org/10.1016/j.sedgeo.2007.01.003

Morton, R. A., & Sallenger, A. H. (2003). Morphological Impacts of Extreme Storms on Sandy Beaches and Barriers. *Journal of Coastal Research*, *19*(3), 560–573.

Nanayama, F., Satake, K., Furukawa, R., Shimokawa, K., Atwater, B. F., Shigeno, K., & Yamaki, S. (2003). Unusually large earthquakes inferred from tsunami deposits along the Kuril trench. *Nature*, *424*(6949), Article 6949. https://doi.org/10.1038/nature01864

Nelson, A. R., Briggs, R. W., Dura, T., Engelhart, S. E., Gelfenbaum, G., Bradley, L.-A., Forman, S. L., Vane, C. H., & Kelley, K. A. (2015). Tsunami recurrence in the eastern Alaska-Aleutian arc: A Holocene stratigraphic record from Chirikof Island, Alaska. *Geosphere*, *11*(4), 1172–1203. https://doi.org/10.1130/GES01108.1

Nelson, A. R., Kelsey, H. M., & Witter, R. C. (2006). Great earthquakes of variable magnitude at the Cascadia subduction zone. *Quaternary Research*, *65*(3), 354–365. https://doi.org/10.1016/j.yqres.2006.02.009

Nelson, A. R., Ota, Y., Umitsu, M., Kashima, K., & Matsushima, Y. (1998). Seismic or hydrodynamic control of rapid late-Holocene sea-level rises in southern coastal Oregon, USA? *The Holocene*, *8*(3), 287–299. https://doi.org/10.1191/095968398668600476

Nelson, A. R., Sawai, Y., Jennings, A. E., Bradley, L.-A., Gerson, L., Sherrod, B. L., Sabean, J., & Horton, B. P. (2008). Great-earthquake paleogeodesy and tsunamis of the past 2000 years at Alsea Bay, central Oregon coast, USA. *Quaternary Science Reviews*, *27*(7–8), 747–768. https://doi.org/10.1016/j.quascirev.2008.01.001

Nelson, A. R., Shennan, I., & Long, A. J. (1996). Identifying coseismic subsidence in tidal-wetland stratigraphic sequences at the Cascadia subduction zone of western North America. *Journal of Geophysical Research: Solid Earth*, *101*(B3), 6115–6135. https://doi.org/10.1029/95JB01051

NHC. (1992). *Preliminary report. Hurricane Winifred. 6—10 October 1992.* p. 8.

NHC. (2021). *Preliminary report Hurricane Sally*. p. 69.

NHC (1993). *Preliminary report Hurricane Calvin 4—9 July 1993.* p. 8.

NOAA. (2004). *Effects of hurricane Isabel on water levels. Data report.* p. 120.

NOAA. (2009). *Hurricane Ike* (p. 42). Water level and meteorological data report.

Novelo, E., Tavera, R., & Ibarra, C. (2007). *Bacillariophyceae from Karstic Wetlands in México*. 137. p. 136.

Núñez-Cornú, F. J., Córdoba, D., Dañobeitia, J. J., Bandy, W. L., Figueroa, M. O., Bartolome, R., Núñez, D., Zamora-Camacho, A., Espíndola, J. M., Castellón, A., Escudero, C. R., Trejo-Gómez, E., de Jesús Escalona-Alcázar, F., Suárez Plascencia, C., Alejandro Nava, F., Mortera, C., & TsuJal Working Group. (2016). Geophysical Studies across Rivera Plate and Jalisco Block, Mexico: TsuJal Project. *Seismological Research Letters*, *87*(1), 59–72. https://doi.org/10.1785/0220150144

Ortiz, M., Kostoglodov, V., K. Singh, S., & Pacheco, J. (2000). New constraints on the uplift of October 9, 1995 Jalisco-Colima earthquake (Mw 8) based on the analysis of tsunami records at Manzanillo and Navidad, Mexico. *Geofísica Internacional*, *39*(4), 349–357. https://doi.org/10.22201/igeof.00167169p.2000.39.4.245

Otvos, E. G. (2011). Hurricane signatures and landforms—Toward improved interpretations and global storm climate chronology. *Sedimentary Geology*, *239*(1), 10–22. https://doi.org/10.1016/j.sedgeo.2011.04.014

Pacheco, J., Singh, S. K., Domínguez, J., Hurtado, A., Quintanar, L., Jiménez, Z., Yamamoto, J., Gutiérrez, C., Santoyo, M., Bandy, W., Guzmán, M., Kostoglodov, V., Reyes, G., & Ramírez, C. (1997). The October 9, 1995 Colima-Jalisco, Mexico Earthquake (Mw 8): An aftershock study and a comparison of this earthquake with those of 1932. *Geophysical Research Letters*, *24*(17), 2223–2226. https://doi.org/10.1029/97GL02070

Padgett, J. S., Engelhart, S. E., Kelsey, H. M., Witter, R. C., & Cahill, N. (2022). Reproducibility and variability of earthquake subsidence estimates from saltmarshes of a Cascadia estuary. *Journal of Quaternary Science*, 1294-1312. https://doi.org/10.1002/jqs.3446

Padilla, H., Torres, M. C., Bélmont, R., García, R., & Báez, A. (2007). Total peroxides and sulfate in rainwater in the Mexican eastern Pacific Ocean during the Climatic Experiment in the Americas Warm Water Pools. *Atmósfera*, *20*(3), 299–305.

Padilla Lozoya, R. (2007). Hurricanes in the State of Colima 1573-1999: Occurrence of risk due to hydrometerorological events (in spanish). *Memories of the 6th International Congress and 12th National of environmental sciences*, 797–802.

Paris, R., Lavigne, F., Wassmer, P., & Sartohadi, J. (2007). Coastal sedimentation associated with the December 26, 2004 tsunami in Lhok Nga, west Banda Aceh (Sumatra, Indonesia). *Marine Geology*, *238*(1), 93–106. https://doi.org/10.1016/j.margeo.2006.12.009

Peterson, C. D., & Darienzo, M. E. (1991). *Discrimination of Climatic, Oceanic and Tectonic Mechanisms of Cyclic Marsh Burial from Alsea Bay, Oregon, U.S.A.* (No. 91–441; Earthquake Hazards in the Pacific Northwest of the United States, p. 53). U.S. Geological Survey.

Plafker, G. (1969). *Tectonics of the March 27, 1964 Alaska earthquake:* (No. 543–I; U.S. Geological Survey Professional Paper 543–I, p. 74).

Plafker, G., & Savage, J. C. (1970). Mechanism of the Chilean Earthquakes of May 21 and 22, 1960. *Geological Society of America Bulletin*, *81*(4), 1001. https://doi.org/10.1130/0016-7606(1970)81[1001:MOTCEO]2.0.CO;2

Qingmin, Y., Kociolek, J. P., & Quanxi, W. (2015). Taxonomic studies of the diatom genus Halamphora (Bacillariophyceae) from the mountainous regions of southwest China, including the description of two new species. *Phytotaxa*, *205*(2), 75. https://doi.org/10.11646/phytotaxa.205.2.1

Ramírez-Herrera, M. T., Bógalo, M. F., Černý, J., Goguitchaichvili, A., Corona, N., Machain, M. L., Edwards, A. C., & Sosa, S. (2016). Historic and ancient tsunamis uncovered on the Jalisco-Colima Pacific coast, the Mexican subduction zone. *Geomorphology*, *259*, 90–104. https://doi.org/10.1016/j.geomorph.2016.02.011

Ramírez-Herrera, M. T., Corona, N., Cerny, J., Castillo-Aja, R., Melgar, D., Lagos, M., Goguitchaichvili, A., Machain, M. L., Vazquez-Caamal, M. L., Ortuño, M., Caballero, M., Solano-Hernandez, E. A., & Ruiz-Fernández, A.-C. (2020). Sand deposits reveal great earthquakes and tsunamis at Mexican Pacific Coast. *Scientific Reports*, *10*(1), 11452. https://doi.org/10.1038/s41598-020-68237-2

Ramírez-Herrera, M. T., Corona, N., Lagos, M., Černý, J., Goguitchaichvili, A., Goff, J., Chagué-Goff, C., Machain, M. L., Zawadzki, A., Jacobsen, G., Carranza-Edwards, A., Lozano, S., & Blecher, L. (2014). Unearthing earthquakes and their tsunamis using multiple proxies: The 22 June 1932 event and a probable fourteenth-century predecessor on the Pacific coast of Mexico. *International Geology Review*, *56*(13), 1584–1601. https://doi.org/10.1080/00206814.2014.951977

Ramírez-Herrera, M. T., Cundy, A. B., Kostoglodov, V., Carranza-Edwards, A., Morales, E., & Metcalfe, S. (2007). Sedimentary record of late-Holocene relative sea-level change and tectonic deformation from the Guerrero Seismic Gap, Mexican Pacific Coast. *The Holocene*, *17*(8), 1211–1220. https://doi.org/10.1177/0959683607085127

Ramírez-Herrera, M. T., Cundy, A. B., Kostoglodov, V., & Ortiz, M. (2009). Late Holocene tectonic land-level changes and tsunamis at Mitla lagoon, Guerrero, Mexico. *Geofísica Internacional*, *48*(2), 195–209.

Ramírez-Herrera, M. T., Kostoglodov, V., & Urrutia-Fucugauchi, J. (2004). Holocene-emerged notches and tectonic uplift along the Jalisco coast, Southwest Mexico. *Geomorphology*, *58*(1–4), 291–304. https://doi.org/10.1016/j.geomorph.2003.07.004

Ramírez-Herrera, M. T., Lagos, M., Hutchinson, I., Kostoglodov, V., Machain, M. L., Caballero, M., Goguitchaichvili, A., Aguilar, B., Chagué-Goff, C., Goff, J., Ruiz-Fernández, A.-C., Ortiz, M., Nava, H., Bautista, F., Lopez, G. I., & Quintana, P. (2012). Extreme wave deposits on the Pacific coast of Mexico: Tsunamis or storms? — A multi-proxy approach. *Geomorphology*, *139–140*, 360–371. https://doi.org/10.1016/j.geomorph.2011.11.002

Ramírez-Herrera, M. T., & Orozco, J. J. Z. (2002). Coastal Uplift and Mortality of Coralline Algae Caused by a 6.3Mw Earthquake, Oaxaca, Mexico. *Journal of Coastal Research*, *18*(1), 75–81.

Ramirez-Herrera, M. T., & Urrutia-Fucugauchi, J. (1999). Morphotectonic zones along the coast of the Pacific continental margin, southern Mexico. *Geomorphology*, *28*(3), 237–250. https://doi.org/10.1016/S0169-555X(99)00016-1

Ramírez-Herrera, M.-T., Romero, D., Corona, N., Nava, H., Torija, H., & Hernández Maguey, F. (2021). The 23 June 2020 Mw 7.4 La Crucecita, Oaxaca, Mexico Earthquake and Tsunami: A Rapid Response Field Survey during COVID-19 Crisis. *Seismological Research Letters*, *92*(1), 26–37. https://doi.org/10.1785/0220200263

Rich, A., & Keller, E. A. (2013). A hydrologic and geomorphic model of estuary breaching and closure. *Geomorphology*, *191*, 64–74. https://doi.org/10.1016/j.geomorph.2013.03.003

Rosales Franco, E., & Camargo Soto, C. (2019). *Carta geológico-minera. Cihuatlán. E13-B42* [Map]. Servicio Geológico Mexicano.

Rothwell, R. G., & Croudace, I. w. (2015). Twenty Years of XRF Core Scanning Marine Sediments: What Do Geochemical Proxies Tell Us? In I. W. Croudace & R. G. Rothwell (Eds.), *Micro-XRF Studies of Sediment Cores: Applications of a non-destructive tool for the environmental sciences* (pp. 25–102). Springer Netherlands. https://doi.org/10.1007/978-94-017-9849-5_2

Roy, P. D., Jonathan, M. P., Macias, Ma. C., Sánchez, J. L., Lozano, R., & Srinivasalu, S. (2012). Geological characteristics of 2011 Japan tsunami sediments deposited along the coast of southwestern Mexico. *Geochemistry*, *72*(1), 91–95. https://doi.org/10.1016/j.chemer.2012.02.003

Rubin, C. M., Horton, B. P., Sieh, K., Pilarczyk, J. E., Daly, P., Ismail, N., & Parnell, A. C. (2017). Highly variable recurrence of tsunamis in the 7,400 years before the 2004 Indian Ocean tsunami. *Nature Communications*, *8*(1), Article 1. https://doi.org/10.1038/ncomms16019

Ruiz-Fernández, A. C., & Hillaire-Marcel, C. (2009). 210Pb-derived ages for the reconstruction of terrestrial contaminant history into the Mexican Pacific coast: Potential and limitations. *Marine Pollution Bulletin*, *59*(4), 134–145. https://doi.org/10.1016/j.marpolbul.2009.05.006

Ruiz-Fernández, A. C., Hillaire-Marcel, C., Ghaleb, B., Soto-Jiménez, M., & Páez-Osuna, F. (2002). Recent sedimentary history of anthropogenic impacts on the Culiacan River Estuary, northwestern Mexico: Geochemical evidence from organic matter and nutrients. *Environmental Pollution*, *118*(3), 365–377. https://doi.org/10.1016/S0269-7491(01)00287-1

Sachs, H. M., Webb, T., & Clark, D. R. (1977). Paleoecological Transfer Functions. *Annual Review of Earth and Planetary Sciences*, *5*(1), 159–178. https://doi.org/10.1146/annurev.ea.05.050177.001111

Sanchez, A. J., & Farreras, S. F. (1987). Tsunami flooding extension for coastal zones of Mexico. *Marine Geodesy*, *11*(2–3), 127–135. https://doi.org/10.1080/15210608709379555

Sawai, Y. (2020). Subduction zone paleoseismology along the Pacific coast of northeast Japan—Progress and remaining problems. *Earth-Science Reviews*, *208*, 103261. https://doi.org/10.1016/j.earscirev.2020.103261

Seminack, C. T., & McBride, R. A. (2018). A life-cycle model for wave-dominated tidal inlets along passive margin coasts of North America. *Geomorphology*, *304*, 141–158. https://doi.org/10.1016/j.geomorph.2017.12.038

Shennan, I., Barlow, N., & Combellick, R. (2013). Paleoseismological Records of Multiple Great Earthquakes in Southcentral Alaska: A 4000-Year Record at Girdwood. In J. T. Freymueller, P. J. Haeussler, R. L. Wesson, & G. Ekström (Eds.), *Geophysical Monograph Series* (pp. 185–199). American Geophysical Union. https://doi.org/10.1029/179GM10

Shennan, I., Garrett, E., & Barlow, N. (2016). Detection limits of tidal-wetland sequences to identify variable rupture modes of megathrust earthquakes. *Quaternary Science Reviews*, *150*, 1–30. https://doi.org/10.1016/j.quascirev.2016.08.003

Shennan, I., & Hamilton, S. (2010). Holocene sea-level changes and earthquakes around Bering Glacier. In *Geological Society of America Special Papers* (Vol. 462, pp. 275–290). Geological Society of America. https://doi.org/10.1130/2010.2462(14)

Shennan, I., Long, A. J., Rutherford, M. M., Innes, J. B., Green, F. M., & Walker, K. J. (1998). Tidal marsh stratigraphy, sea-level change and large earthquakes—II: Submergence events during the last 3500 years at netarts bay, Oregon, USA. *Quaternary Science Reviews*, *17*(4), 365–393. https://doi.org/10.1016/S0277-3791(97)00055-3

Shennan, I., Scott, D. B., Rutherford, M., & Zong, Y. (1999). Microfossil analysis of sediments representing the 1964 earthquake, exposed at Girdwood Flats, Alaska, USA. *Quaternary International*, *60*(1), 55–73. https://doi.org/10.1016/S1040-6182(99)00007-5

Siqueiros Beltrones, D. A., Lopez-Fuerte, F. O., & Garate-Lizarraga, I. (2005). Structure of Diatom Assemblages Living on Prop Roots of the Red Mangrove (Rhizophora mangle) from the West Coast of Baja California Sur, Mexico. *Pacific Science*, *59*(1), 79–96. https://doi.org/10.1353/psc.2005.0014

Siqueiros-Beltrones, D. A., Argumedo-Hernández, U., & López-Fuerte, F. O. (2017). Diversity of benthic diatoms in the Guerrero Negro Lagoon (El Vizcaíno Biosfere Reserve), Baja California Peninsula, Mexico. *Revista Mexicana de Biodiversidad*, *88*(1), 21–35. https://doi.org/10.1016/j.rmb.2017.01.026

Siqueiros-Beltrones, D. A., López-Mejía, D., & Gutiérrez-Mendieta, F. (2020). High species richness of epiphytic Mastogloia (Mastogloiales: Bacillariophyceae) on Thalassia testudinum along the coast of Campeche, southern Gulf of Mexico. *Revista Mexicana de Biodiversidad*, *91*(0). https://doi.org/10.22201/ib.20078706e.2020.91.2976

SMN. (2021). *Manzanillo tide gauge data*. Servicio Mareografico Nacional, México. http://www.mareografico.unam.mx

Soria, J. L. A., Switzer, A. D., Pilarczyk, J. E., Siringan, F. P., Khan, N. S., & Fritz, H. M. (2017). Typhoon Haiyan overwash sediments from Leyte Gulf coastlines show local spatial variations with hybrid storm and tsunami signatures. *Sedimentary Geology*, *358*, 121–138. https://doi.org/10.1016/j.sedgeo.2017.06.006

Spotila, J. A., Marshall, J., DePew, K., Prince, P. S., & Kennedy, L. (2015). Potential for Geologic Records of Coseismic Uplift and Megathrust Rupture along the Nicoya Peninsula, Costa Rica. *Journal of Coastal Research*, 387–396. https://doi.org/10.2112/JCOASTRES-D-14-00151.1

Szabó, K., Kiss, K. T., Ector, L., Kecskés, M., & Ács, É. (2004). Benthic diatom flora in a small Hungarian tributary of River Danube (Rakos-stream). *Algological Studies/Archiv Für Hydrobiologie, Supplement Volumes*, *111*, 79–94. https://doi.org/10.1127/1864-1318/2004/0111-0079

Takashimizu, Y., Urabe, A., Suzuki, K., & Sato, Y. (2012). Deposition by the 2011 Tohoku-oki tsunami on coastal lowland controlled by beach ridges near Sendai, Japan. *Sedimentary Geology*, *282*, 124–141. https://doi.org/10.1016/j.sedgeo.2012.07.004

Trejo-Gómez, E., Ortiz, M., & Núñez-Cornú, F. J. (2015). Source Model of the October 9, 1995 Jalisco-Colima Tsunami as constrained by field survey reports, and on the numerical simulation of the tsunami. *Geofísica Internacional*, *54*(2), 149–159. https://doi.org/10.1016/j.gi.2015.04.010

Troels-Smith, J. (1955). Karakterisering af lose jordater (Characterisation of Unconsolidated Sediments). *Danmarks Geologiske Undersogelse*, *3*, 39–73.

Vaasma, T. (2008). Grain-size analysis of lacustrine sediments: A comparison of pre-treatment methods. *Estonian Journal of Ecology*, *57*(4), 231. https://doi.org/10.3176/eco.2008.4.01

Vélez, M. I., Hooghiemstra, H., Metcalfe, S., Wille, M., & Berrío, J. C. (2006). Late Glacial and Holocene environmental and climatic changes from a limnological transect through Colombia, northern South America. *Palaeogeography, Palaeoclimatology, Palaeoecology*, *234*(1), 81–96. https://doi.org/10.1016/j.palaeo.2005.10.020

Vos, P. C., & de Wolf, H. (1993). Diatoms as a tool for reconstructing sedimentary environments in coastal wetlands; methodological aspects. *Hydrobiologia*, *269*(1), 285–296. https://doi.org/10.1007/BF00028027

Wang, K., Hu, Y., & He, J. (2012). Deformation cycles of subduction earthquakes in a viscoelastic Earth. *Nature*, *484*(7394), 327–332. https://doi.org/10.1038/nature11032

Watanabe, M., Bricker, J. D., Goto, K., & Imamura, F. (2017). Factors responsible for the limited inland extent of sand deposits on Leyte Island during 2013 Typhoon Haiyan. *Journal of Geophysical Research: Oceans*, *122*(4), 2795–2812. https://doi.org/10.1002/2016JC012023

Wilson, R., Hemphill-Haley, E., Jaffe, B., Richmond, B., Peters, R., Graehl, N., Kelsey, H., Leeper, R., Watt, S., McGann, M., Hoirup, D., Chagué-Goff, C., Goff, J., Caldwell, D., & Loofbourrow, C. (2014). *The search for geologic evidence of distant-source tsunamis using new field data in California* (Open-File Report No. 229; The SAFRR (Science Application for Risk Reduction) Tsunami Scenario). U.S. Geological Survey.

Yan, Y. T., Chua, S., DeCarlo, T. M., Kempf, P., Morgan, K. M., & Switzer, A. D. (2021). Core-CT: A MATLAB application for the quantitative analysis of sediment and coral cores from X-ray computed tomography (CT). *Computers & Geosciences*, *156*, 104871. https://doi.org/10.1016/j.cageo.2021.104871

Yáñez-Arancibia, A., Day, J. W., Sánchez-Gil, P., Day, J. N., Lane, R. R., Zárate-Lomelí, D., Vásquez, H. A., Rojas-Galaviz, J. L., & Ramírez-Gordillo, J. (2014). Ecosystem functioning: The basis for restoration and management of a tropical coastal lagoon, Pacific coast of Mexico. *Ecological Engineering*, *65*, 88–100. https://doi.org/10.1016/j.ecoleng.2013.03.007

Zobin, V. M., & Ventura-Ramirez, J. F. (1998). The Macroseismic Field Generated by the Mw 8.0 Jalisco, Mexico, Earthquake of 9 October 1995. *Bulletin of the Seismological Society of America*, *88*(3), 703–711.

Zong, Y. (1997). Implications of Paralia Sulcata Abundance in Scottish Isolation Basins. *Diatom Research*, *12*(1), 125–150. https://doi.org/10.1080/0269249X.1997.9705407

Zong, Y., Lloyd, J. M., Leng, M. J., Yim, W. W.-S., & Huang, G. (2006). Reconstruction of Holocene monsoon history from the Pearl River Estuary, southern China, using diatoms and carbon isotope ratios. *The Holocene*, *16*(2), 251–263. https://doi.org/10.1191/0959683606hl911rp

Zong, Y., & Sawai, Y. (2015). Diatoms. In I. Shennan, A. J. Long, & B. P. Horton (Eds.), *Handbook of Sea-Level Research* (pp. 233–248). John Wiley & Sons, Ltd. https://doi.org/10.1002/9781118452547.ch15

Zong, Y., Shennan, I., Combellick, R. A., Hamilton, S. L., & Rutherford, M. M. (2003). Microfossil evidence for land movements associated with the AD 1964 Alaska earthquake. *The Holocene*, *13*(1), 7–20. https://doi.org/10.1191/0959683603hl590rp

Zuber, A., Álvarez, M.-C., Mendoza, E., Díaz-Flores, M. Á., Galicia-Pérez, M., & Torres-Orozco, E. (2022). Monitoring Beach Shape Development and Sediment Dynamics on a Sandy Beach with Low Anthropogenic Influence. *Land*, *11*(12), Article 12. https://doi.org/10.3390/land11122219